The Astrophysical Journal Supplement Series, 237:31 (17pp), 2018 August https://doi.org/10.3847/1538-4365/aace58

First Data Release of the COSMOS Lyα Mapping and Tomography Observations: 3D Lyα Forest Tomography at $2.05 < z < 2.55$

Khee-Gan Lee[1,21], Alex Krolewski[2], Martin White[1,2], David Schlegel[1], Peter E. Nugent[1,2], Joseph F. Hennawi[3], Thomas Müller[4], Richard Pan[2], J. Xavier Prochaska[5,6], Andreu Font-Ribera[7], Nao Suzuki[8], Karl Glazebrook[9], Glenn G. Kacprzak[9], Jeyhan S. Kartaltepe[10], Anton M. Koekemoer[11], Olivier Le Fèvre[12], Brian C. Lemaux[12,13], Christian Maier[14], Themiya Nanayakkara[15], R. Michael Rich[16], D. B. Sanders[17], Mara Salvato[18], Lidia Tasca[12], and Kim-Vy H. Tran[19,20]

[1] Lawrence Berkeley National Laboratory, 1 Cyclotron Road, Berkeley, CA 94720, USA; kglee@lbl.gov
[2] Department of Astronomy, University of California at Berkeley, New Campbell Hall, Berkeley, CA 94720, USA
[3] Department of Physics, Broida Hall, University of California at Santa Barbara, Santa Barbara, CA 93106, USA
[4] Max Planck Institute for Astronomy, Königstuhl 17, D-69117 Heidelberg, Germany
[5] Department of Astronomy and Astrophysics, University of California at Santa Cruz, 1156 High Street, Santa Cruz, CA 95064, USA
[6] University of California Observatories, Lick Observatory, 1156 High Street, Santa Cruz, CA 95064, USA
[7] Department of Physics and Astronomy, University College London, Gower Street, London, WC1E 6BT, UK
[8] Kavli Institute for the Physics and Mathematics of the Universe (IPMU), The University of Tokyo, Kashiwano-ha 5-1-5, Kashiwa-shi, Chiba, Japan
[9] Swinburne University of Technology, Victoria 3122, Australia
[10] School of Physics and Astronomy, Rochester Institute of Technology, 84 Lomb Memorial Drive, Rochester, NY 14623, USA
[11] Space Telescope Science Institute, 3700 San Martin Drive, Baltimore MD 21218, USA
[12] Aix Marseille Université, CNRS, LAM (Laboratoire d'Astrophysique de Marseille) UMR 7326, F-13388, Marseille, France
[13] Department of Physics, University of California, Davis, One Shields Ave., Davis, CA 95616, USA
[14] University of Vienna, Department of Astrophysics, Tuerkenschanzstrasse 17, A-1180 Vienna, Austria
[15] Leiden Observatory, Leiden University, P.O. Box 9513, 2300 RA Leiden, The Netherlands
[16] Department of Physics and Astronomy, University of California at Los Angeles, Los Angeles, CA 90095, USA
[17] Institute for Astronomy, University of Hawaii, 2680 Wooodlawn Drive, Honolulu, HI 96822, USA
[18] Max Planck Institute for Extraterrestrial Physics, Gießenbachstrae 1, D-85741 Garching bei München, Germany
[19] School of Physics, University of New South Wales, Kensington, Australia
[20] George P. and Cynthia Woods Mitchell Institute for Fundamental Physics and Astronomy, and Department of Physics and Astronomy, Texas A&M University, College Station, TX 77843, USA
Received 2017 October 10; revised 2018 May 29; accepted 2018 June 12; published 2018 August 2

Abstract

Faint star-forming galaxies at $z \sim 2$–3 can be used as alternative background sources to probe the Lyα forest in addition to quasars, yielding high sightline densities that enable 3D tomographic reconstruction of the foreground absorption field. Here, we present the first data release from the COSMOS Lyα Mapping And Tomography Observations (CLAMATO) Survey, which was conducted with the LRIS spectrograph on the Keck I telescope. Over an observational footprint of 0.157 deg^2 within the COSMOS field, we used 240 galaxies and quasars at $2.17 < z < 3.00$, with a mean comoving transverse separation of 2.37 h^{-1} Mpc, as background sources probing the foreground Lyα forest absorption at $2.05 < z < 2.55$. The Lyα forest data was then used to create a Wiener-filtered tomographic reconstruction over a comoving volume of $3.15 \times 10^5\ h^{-3}$ Mpc^3 with an effective smoothing scale of 2.5 h^{-1} Mpc. In addition to traditional figures, this map is also presented as a virtual-reality visualization and manipulable interactive figure. We see large overdensities and underdensities that visually agree with the distribution of coeval galaxies from spectroscopic redshift surveys in the same field, including overdensities associated with several recently discovered galaxy protoclusters in the volume. Quantitatively, the map signal-to-noise is $S/N^{wiener} \approx 3.4$ over a 3 h^{-1}Mpc top-hat kernel based on the variances estimated from the Wiener filter. This data release includes the redshift catalog, reduced spectra, extracted Lyα forest pixel data, and reconstructed tomographic map of the absorption. These can be downloaded from Zenodo (10.5281/zenodo.1292459).

Key words: intergalactic medium – large-scale structure of universe – quasars: absorption lines – surveys – techniques: spectroscopic

Supporting material: animation, interactive figures, machine-readable table

1. Introduction

The Lyα forest absorption from residual, diffuse, H I in the intergalactic medium (IGM) is a well-established tracer of cosmological large-scale structure (e.g., Croft et al. 1998; McDonald et al. 2006; Slosar et al. 2011; Busca et al. 2013). In particular, since the hydrogen Lyα transition (rest-frame wavelength $\lambda = 1215.67$ Å) redshifts into the optical atmospheric window at $z \gtrsim 2$, this makes the Lyα forest a particularly important probe at redshifts that are otherwise challenging to access through methods such as galaxy redshift surveys or gravitational weak lensing, which at the time of writing are typically limited to $z < 1$.

As the brightest ultraviolet sources in the distant universe, quasars have been the traditional background objects against which the absorption of the IGM Lyα forest have been studied along the foreground lines of sight. Due to the comparative rarity of quasars on the sky, however, these studies have generally been confined to one-dimensional lines of sight

[21] Hubble Fellow.

directly in front of each quasar (but see Rollinde et al. 2003; D'Odorico et al. 2006, for early studies using closely separated quasar sightlines).

More recently, the Lyα forest component of the BOSS survey (Eisenstein et al. 2011; Dawson et al. 2013) has systematically pursued sufficiently high number densities of $z > 2$ quasars such that it becomes possible to cross-correlate the absorption seen in different quasar sightlines (Slosar et al. 2011), although the mean transverse separation between sightlines is relatively large ($\langle d_\perp \rangle \sim 20\,h^{-1}$ Mpc). This was, however, more than sufficient for achieving BOSS's primary survey goal of measuring the baryon acoustic oscillation signal in the 3D Lyα forest clustering (Busca et al. 2013; Kirkby et al. 2013; Slosar et al. 2013; Font-Ribera et al. 2014; Delubac et al. 2015; Bautista et al. 2017; du Mas des Bourboux et al. 2017).

By targeting fainter background sources than the $g < 22$ quasars observed by BOSS, the mean sightline separation can be decreased to probe smaller scales, although the quasar luminosity function is too shallow to be worth the steep increase in observational resources needed: based on the Palanque-Delabrouille et al. (2013a) luminosity function, for example, $g < 24$ quasars at $2.4 < z < 2.8$ that can probe the $z \sim 2.3$ Lyα forest only achieve target densities of $\sim$80 deg^2 or mean separations of $\langle d_\perp \rangle \sim 7.5\,h^{-1}$ Mpc. In addition to quasars, it is possible to dramatically increase sightline densities by targeting UV-emitting star-forming galaxies at $z > 2$, often referred to as "Lyman-Break Galaxies" (LBGs) due to their original selection method (Steidel et al. 1996). Lee et al. (2014a) calculated, for example, that a $g = 24.5$ survey limit leads to $\sim$1500 deg^{-2} of sightlines with a mean spacing of $\langle d_\perp \rangle \sim 2.5\,h^{-1}$ Mpc.

With background sources separated by only several transverse Mpc, it becomes interesting to carry out a tomographic reconstruction to recover the 3D Lyα forest absorption field on spatial resolutions that resolve the cosmic web. This concept was first proposed in Pichon et al. (2001) and Caucci et al. (2008), while Lee et al. (2014a) studied the observational feasibility and argued that present-day instrumentation should be capable of implementing IGM tomography down to scales of 2–3 h^{-1} Mpc (but see Ozbek et al. 2016 for an application of IGM tomography on larger-scale BOSS data). Subsequently, pilot observations on the Keck telescope were reported in Lee et al. (2014b) and expanded, with additional data, into an analysis of a $z = 2.45$ galaxy protocluster that was previously discovered within the tomography field (Lee et al. 2016). Meanwhile, Stark et al. (2015a) and Stark et al. (2015b) used numerical simulations to quantify the utility of such IGM maps for identifying galaxy protoclusters and cosmic voids, respectively, at $z \sim 2.5$ (although see Cai et al. 2016, 2017, for complementary studies). Schmittfull & White (2016) then showed that IGM tomographic maps could be used to refine photometric redshifts of foreground galaxies with large halo masses. Later, Lee & White (2016) demonstrated that upcoming IGM tomography surveys and facilities will be capable of recovering the geometric cosmic environments of large-scale structure (i.e., voids, sheets, filaments, and nodes) from the $z \sim 2.5$ IGM at comparable fidelity to $z \sim 0.4$ galaxy redshift survey maps. Krolewski et al. (2017) expanded this to demonstrate that large-scale structure filaments can be sufficiently resolved by upcoming IGM tomography surveys to allow constraints on galaxy-filament alignments with samples of > 1000 coeval galaxies.

In this Supplement, we present the first public data release of the COSMOS Lyα Mapping And Tomographic Observations (CLAMATO) survey.[22] This is an observational program, conducted with the LRIS spectrograph (Oke et al. 1995; Steidel et al. 2004) on the Keck I telescope designed as the first systematic attempt to observe relatively faint star-forming galaxies at $z \sim 2$–3 at high area densities ($\sim$1000 deg^{-2}) in order to carry out Lyα forest tomography of the foreground IGM. The current release incorporates observations over 0.157 square degrees of the COSMOS field obtained with the Keck I telescope from 2014 through 2017.

The primary product in this release is the tomographically reconstructed 3D map of the $2.05 < z < 2.55$ Lyα forest absorption derived from 240 background galaxies and QSOs within the field, but we also include the spectra and estimated redshifts of 437 objects that were successfully reduced. The various products have been made available in a public webpage,[23] and are described in Appendix A.

This paper will act as a reference for multiple science analyses with the CLAMATO data that are currently in preparation, including the first detection of cosmic voids at $z > 2$ (Krolewski et al. 2018), the cross-correlation of Lyα forest absorption with foreground galaxies from various spectroscopic redshift catalogs in the same field, and the analysis of the multiple clusters and protoclusters that fall within our current volume. While the current footprint is likely too small for cosmic web analyses due to boundary effects (Lee et al. 2016), it should be sufficient to begin the first attempts to study the scalar properties of large-scale structure at this epoch. This data set is also intended as a value-added resource for other researchers studying this heavily observed cosmic volume, as well as a reference data set to prepare the Lyα forest tomography science cases for upcoming instruments such as the *Subaru* Prime Focus Spectrograph (Sugai et al. 2015), the Maunakea Spectroscopic Explorer (McConnachie et al. 2016a), the Thirty Meter Telescope Wide-Field Optical Spectrograph (Skidmore et al. 2015), and the European Extremely Large Telescope Multi-Object Spectrograph (Hammer et al. 2016).

In this paper, we assume a concordance flat ΛCDM cosmology, with $\Omega_M = 0.31$, $\Omega_\Lambda = 0.69$ and $H_0 = 70\,\mathrm{km\,s^{-1}\,Mpc^{-1}}$. The exact choice of cosmology does not significantly affect our resulting tomographic reconstruction—which is intended for galaxy evolution purposes—since it only affects the conversion of redshift and angular separation into comoving distances. Future cosmological analyses would need to be more careful about the choice of cosmology, or indeed carry out analyses directly on the pixel data rather than using a tomographic reconstruction.

2. Survey Design and Target Selection

2.1. Survey Field

As CLAMATO is the first attempt at mapping large-scale structure using IGM tomography at $z \sim 2$, we had to choose a well-studied extragalactic field that offers sufficiently deep imaging, and ideally, spectroscopy to select UV-bright star-forming galaxies with sufficient depth ($g > 24$) to have mean

[22] Website: http://clamato.lbl.gov.
[23] 10.5281/zenodo.1292459.

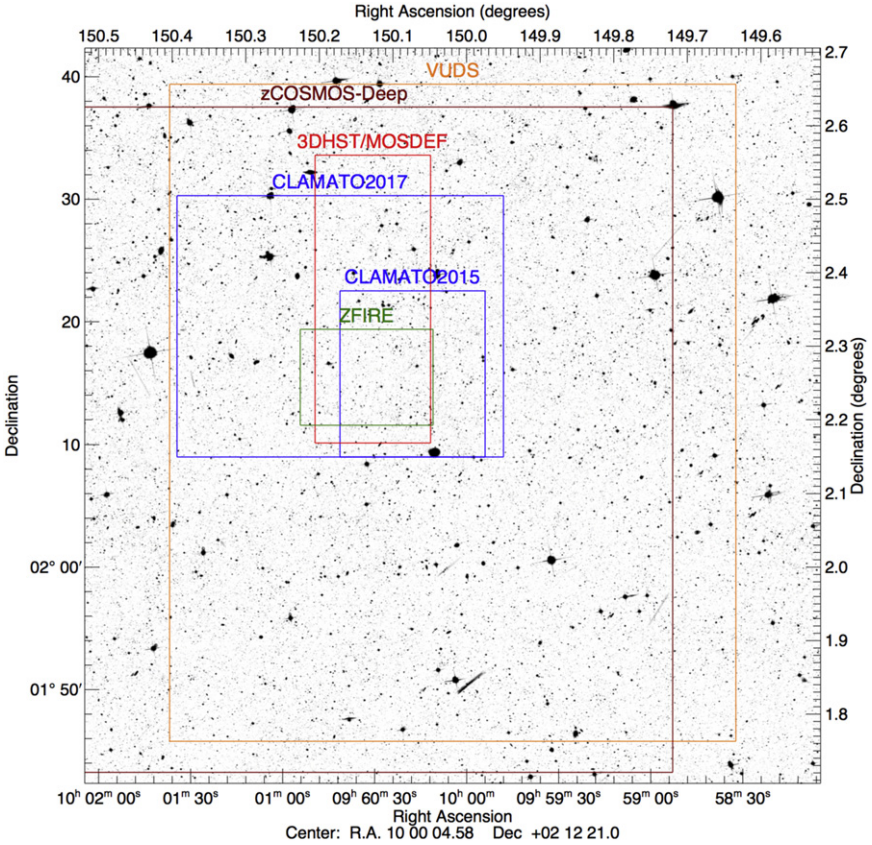

Figure 1. CLAMATO in context: this shows a *Hubble Space Telescope* ACS F814W mosaic (Koekemoer et al. 2007) of the central regions in the COSMOS field, with the footprint of the CLAMATO tomographic map indicated in blue (both the current paper and 2015 version, Lee et al. 2016). Also shown are the approximate footprints for other spectroscopic redshift surveys that probe similar redshifts, such as 3D-*HST* (Momcheva et al. 2016) and MOSDEF (Kriek et al. 2015) in red, zCOSMOS-Deep (Lilly et al. 2007) in brown, VUDS (Le Fèvre et al. 2015) in orange, and ZFIRE (Nanayakkara et al. 2016) in green. The overall ACS footprint used for the Capak et al. (2007) base *i*-band catalog is larger than the field shown here.

separations of $\sim 2'$–$3'$. At the same time, we desired a large enough footprint to cover large-scale structure on $\gtrsim 10$ cMpc scales in the transverse dimension, i.e., an extragalactic field spanning $> 10'$. This left the 2 deg^2 COSMOS field (Scoville et al. 2007) as the obvious candidate accessible from the Northern Hemisphere, which also had the additional advantage of multiple deep spectroscopic surveys that cover our target redshifts, e.g., zCOSMOS (Lilly et al. 2007), VUDS (Le Fèvre et al. 2015), MOSDEF (Kriek et al. 2015), and ZFIRE (Nanayakkara et al. 2016). The locations of these fields relative to CLAMATO are indicated in Figure 1. Currently, CLAMATO has fully covered the ZFIRE footprint and approximately 80% of the MOSDEF footprint within COSMOS.

2.2. Target Catalogs

The target selection for CLAMATO is aimed at exploiting the rich availability of spectroscopic and multi-wavelength imaging data within the COSMOS field (Scoville et al. 2007) in order to maximize the area density and spatial homogeneity of g-band (rest-frame UV at $z \sim 2$–3) sources that can probe the foreground Lyα forest absorption within a narrow redshift range of $z \sim 2$–3. The COSMOS field has high-quality multi-wavelength photometric redshifts (Ilbert et al. 2009; Laigle et al. 2016), as well as large numbers of spectroscopic redshifts that have already been obtained within our desired footprint and redshift range. We will also retarget objects that have been observed by the zCOSMOS-Deep (Lilly et al. 2007) and VUDS (Le Fèvre et al. 2015), even though their spectra, in principle, cover our desired wavelength range (3700 Å $< \lambda <$ 4300 Å). This is because the spectra from both these surveys have a spectral resolution of $R \sim 200$ at these wavelengths, which means that the resolution element is equivalent to a 16 h^{-1} Mpc line-of-sight comoving distance at $z = 2.3$; this is far too coarse for our desired spatial resolution of several Mpc.

This data described in this paper represent three distinct target selection iterations: pilot observations from (2014–2015), 2016, and 2017. The overall target selection algorithm was the same over the different observing seasons, but the input catalog was updated at the beginning of each of the aforementioned epochs to exploit the best available data at that point.

Initially, we created a master raw catalog that includes a superset of objects in the COSMOS field with $g < 25.2$ at $2.0 < z < 3.5$, which would act as a basis for target selection. As a starting point, we use the compilation of available spectroscopic redshifts within the 2 deg^2 COSMOS field by M. Salvato et al. (2018, in preparation), which includes 68116 unique redshifts from all sources.[24] At our redshift of interest ($z \sim 2$–3), most spectroscopic sources within this compilation are from the zCOSMOS-Deep survey (Lilly et al. 2007). We then supplemented this with preliminary versions of the VUDS (Le Fèvre et al. 2015), MOSDEF (Kriek et al. 2015), and

[24] We used the 2015 April iteration of this catalog.

ZFIRE (Nanayakkara et al. 2016) spectroscopic catalogs, as well as the 3D-*HST* grism redshifts (Momcheva et al. 2016).

In addition to spectroscopic redshift catalogs, we also use the Ilbert et al. (2009) *i*-band-selected photometric redshift catalog, which in turn is based on the Capak et al. (2007) imaging multi-wavelength catalog in the 2 deg^2 COSMOS field. The photometric redshifts from Ilbert et al. (2009) exploit a wide array of multi-wavelength data, with up to 30 bands ranging from the ultraviolet to radio wavelengths. This yields a relatively accurate redshift estimate and low catastrophic failure rate. In 2017, we supplemented this with the Davidzon et al. (2017) photometric redshift catalog, which is a high-redshift optimization of the NIR-selected catalog of Laigle et al. (2016) and provides more accurate photometric redshifts than Ilbert et al. (2009). However, since this is a NIR-selected catalog based on z^{++}-band and *YJHK*$_s$-band selection, it does not provide good completeness for rest-frame UV-bright objects that require an optical detection. We therefore continue to use the Ilbert et al. (2009) catalog to provide a baseline of objects and simply replace the photometric redshift values by the Davidzon et al. (2017) version with objects that have a match. For part of the field, we were also able to use the ZFOURGE medium-band redshifts (Straatman et al. 2016), which should provide superior photometric redshifts at our target redshift; these were also incorporated, where available, by overriding the Ilbert et al. (2009) and Davidzon et al. (2017) redshifts.

2.3. Selection Algorithm

The target selection was then carried out as a two-step procedure: initial selection and prioritization of possible targets, followed by slitmask design, with slit assignments guided by the target priorities. Note the difference between these steps: target *selection* involves identifying all objects that might possibly be used for our purposes and prioritizing them based on redshift, magnitude, and probability of success (e.g., spectroscopic versus photometric redshift from surveys of varying quality); but not all of these will be *assigned* slits due to packing constraints on each slitmask.

In the selection/prioritization step, we fed the combined spectroscopic and photometric catalog to an algorithm designed to initially select and prioritize background g-band sources to homogeneously probe a fixed Lyα absorption redshift z_α. In our case, since we aimed to probe a finite redshift range at $z \sim 2.3$, we ran the target selection algorithm at $z_\alpha = 2.25$ and $z_\alpha = 2.45$ and collated the targets. This algorithm first divides the field into square cells of 2.75 arc-minutes on a side, approximately our desired sightline separation. For each cell, it selects candidate background sources at redshifts

$$(1 + z_\alpha)1216/1195 - 1 < z_{\rm bg} < (1 + z_\alpha)1216/1040 - 1,$$

that could probe the forest absorption at z_α in the rest-frame 1040 Å $< \lambda <$ 1216 Å spectral region between the Lyα and Lyβ transitions. It then gives the highest priority to the "bright" sources (defined as $g < [24.2, 24.4]$ at $z_\alpha = [2.25, 2.45]$, respectively) that have spectroscopic redshifts, while faint or photometric redshift-selected objects are down-prioritized. Due to slit-packing constraints, the algorithm deprioritizes relatively bright sources if another, brighter, high-confidence target is within the same cell, while fainter or photometric redshift targets might receive relatively high priority in the absence of other suitable background sources within its 2.75 arc-minute cell. To take into account the possibility that slit collisions from targets in other cells might clobber the highest-priority source within a given cell, the algorithm selected multiple sources per cell (with decreasing priority) where available. This procedure selected targets as faint as $g = 25.3$ in regions with a paucity of better sources, but such faint targets were assigned a commensurately low priority.

The initial selection of sources, and their priority rankings from this algorithm, were then fed into the AUTOSLIT3 software[25] in order to manually design LRIS slitmasks. For the slitmask design, we chose slits with 1″ width and a minimum length of 6.″5 separated by 1″. The initial slit assignment was automatically carried out by AUTOSLIT3 based on the priorities assigned by the initial target selection algorithm, which we then refined in order to maximize homogeneity of bright sources and uniformity of redshift coverage within our desired $2 \lesssim z_\alpha \lesssim 2.5$ absorption redshift range. This manual refinement included modifying the position angle of the slitmask (up to ±6–7 degrees[26]) in order to mitigate slit collisions between high-priority targets. We also overlapped the slitmasks slightly in the R.A. direction, in order to ensure at least $\lambda > 3700$ Å spectra coverage for all sources. For each $7' \times 5'$ LRIS slitmask, we were able to assign ∼20–25 science slits. Due to slit-packing constraints and the necessity of having at least four alignment stars within each slitmask, this in fact included only ∼80% of the high-priority targets we would have liked to observe within our desired redshift range—we frequently had slit collisions between high-priority sources (or with box stars), while available slits elsewhere had no high-priority targets and were assigned to low-priority targets. A higher slit-packing density would have allowed a slight improvement in sightline density at the same depth, or an increase in the absorption redshift range beyond the $2.05 < z < 2.55$ charted in this survey.

We designed a uniform set of slitmasks to cover our entire survey footprint (Figure 2), but also supplemented these with additional slitmasks (Table 1)—designed and observed in subsequent observing seasons after the initial pass— to increase sightline sampling in particular regions of interest, or to make up for shortfalls in sightline density after the initial round of observations.

3. Observations and Data Reduction

The CLAMATO observations were carried out using the LRIS spectrograph (Oke et al. 1995; Steidel et al. 2004) on the Keck I telescope at Maunakea, Hawai'i. The observations described in these papers were carried out in the spring semesters of 2014–2017 via a total time allocation of 15.5 nights, of which 13.5 nights were allocated by the University of California Time Allocation Committee (TAC) and 2 nights were from the Keck/*Subaru* exchange time given by the National Astronomical Observatory of Japan TAC. Out of this overall allocation, we achieved approximately 60 hr of on-sky integration.[27]

For CLAMATO, we focused on the LRIS blue channel, which covers the 3700 Å $< \lambda <$ 4400 Å wavelength range corresponding to rest-frame Lyα at $2.1 \lesssim z_\alpha \lesssim 2.6$, our redshifts of interest. All our observations used the 600-line

[25] https://www2.keck.hawaii.edu/inst/lris/autoslit_WMKO.html

[26] The notable exception is slitmask sp18L, which was designed with a 43° position angle in an attempt cover a specific gap in the sightline coverage.

[27] On any given night, from Hawai'i, there was at most 5.5 hr in which the COSMOS field could be observable below our threshold of airmass 1.5.

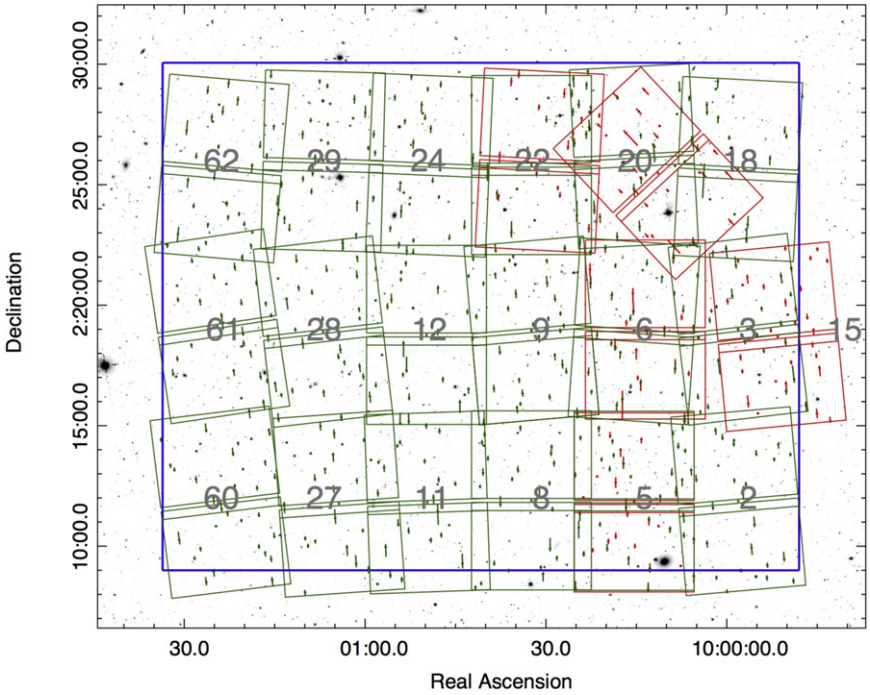

Figure 2. Slits and footprints of the 23 Keck I/LRIS slitmasks observed during the 2014–2017 CLAMATO campaign in the COSMOS field, overlaid on top of the deep *Hubble Space Telescope* ACS F814W mosaic of the same field (Koekemoer et al. 2007). The blue box indicates the footprint of the reconstructed tomographic map from the $2.15 < z < 2.55$ Lyα forest absorption. Most of the slitmasks were designed to achieve a uniform survey layer (dark green), while several were "special" slitmasks (red) designed to obtain additional sightlines in specific regions; see Table 1. The numbers in gray approximately label the field positions.

grism blazed at 4000 Å in the blue channel, which offers spectral resolution of $R \equiv \lambda/\Delta\lambda \approx 1100$ with $1''$ slits. This translates to a spectral FWHM ≈4 Å or a line-of-sight spatial resolution of 3 h^{-1} Mpc at $z \sim 2.3$, which is a good match for our desired sightline separation. The red channel was used primarily to assist in object identification and redshift estimation. On the first two nights of the 2014 observations, we used the d500 dichroic to split the red photons into the red camera with 600-line grating blazed at 7500 Å, but this was deemed to have too short a wavelength coverage, so in all subsequent observations we used the d560 dichroic with the 400-line grating blazed at 8500 Å. This allowed better spectral coverage in the red (up to ≈9000 Å) at the expense of lower spectral resolution, which is still sufficient for spectral identification.

The observations were carried out at a mean seeing of $\approx 0\farcs7$. In seeing conditions of $<0\farcs8$ seeing, we typically exposed for a total of 7200 s per "normal" survey slitmask, but this was increased up to 14400s in sub-optimal seeing in order to achieve roughly homogeneous minimum signal-to-noise over all our data. For "special" slitmasks designed to plug gaps in sightline coverage from the "normal" slitmasks, we integrated longer to build up signal-to-noise on fainter background sources, up to 19800s (however, many of these longer integrations were to make up for inferior seeing conditions). Seeing conditions that were consistently above $1\farcs0$ were deemed unusable for CLAMATO, at which point we moved on to backup targets unrelated to IGM tomography. The individual exposures were typically 1800s on the blue channel but only 860s on the red channel, in order to reduce the number of cosmic ray hits in the latter's thick fully depleted CCDs (Rockosi et al. 2010). In practice, we carried out quick reductions during the observing run to gauge data quality, and occasionally obtained further integrations on a slitmask if the signal-to-noise was considered inadequate after the standard 7200 s. A number of the objects were assigned slits in the overlap region between two (or more) slitmasks, and therefore received considerably more exposure time. Over this observing campaign, we observed 18 "regular" slitmasks over the survey footprint, and also 5 "special" slitmasks (Table 1 and Figure 2).

The data were reduced with the LowRedux routines from the XIDL software package.[28] After the initial flat-fielding, slit definition and sky subtraction, we co-added the 2D images of the individual exposures before tracing the 1D spectra. We found that this helps the extraction of faint source spectra, rather than co-adding the 1D spectra extracted from the individual exposure frames. Due to instrument flexure, this was generally feasible only with exposures observed within the same night or adjacent nights. In cases where data from different observing epochs could not directly be co-added in 2D, the spectra from each epoch were co-added in 1D after extraction and flux calibration. There were 56 objects that were targeted in more than one slitmask, and their 1D spectra were similarly co-added in the same way after initial reduction and extraction. One particular object (ID# 00954) received as much as 11.5 hr of integration from being in the overlap region of four slitmasks.

From the 23 unique slitmasks observed in the 2014–2017 CLAMATO campaign (Table 1), we successfully reduced and extracted 437 spectra from the blue channel (not including 19 spectra from unrelated "filler" programs). We also reduced the red channel but the extraction proved to be more challenging than that in the blue, yielding only 185 corresponding red spectra. The spectra were visually inspected and compared with common line transitions and spectral templates, particularly the Shapley et al. (2003) composite LBG template, in order to

[28] http://www.ucolick.org/~xavier/LowRedux

Table 1
CLAMATO Data Release 1 Slitmasks

Mask name[a]	α (J2000)[b]	δ (J2000)[b]	Exposure Time (s)	Year Observed	Remarks
cpilot09	10 00 33.067	+02 20 50.58	7200	2014	Uniform Survey Mask
cpilot08	10 00 32.404	+02 13 48.01	7200	2014	Uniform Survey Mask
cpilot05	10 00 15.365	+02 13 47.01	7200	2015	Uniform Survey Mask
cpilot06	10 00 14.834	+02 20 48.73	7200	2015	Uniform Survey Mask
cpilot02	09 59 58.765	+02 13 45.55	7200	2015	Uniform Survey Mask
cpilot03	09 59 59.014	+02 20 53.21	10800	2015	Uniform Survey Mask
cpilot12	10 00 49.818	+02 20 40.01	16200	2014/2016	Uniform Survey Mask
pc06	10 00 13.503	+02 20 53.43	7200	2015	Targeted at $z = 2.10$ Protocluster
npc05	10 00 15.358	+02 13 43.08	19800	2016	Targeted at $z = 2.30$ Galaxy Overdensity
c16_11	10 00 49.944	+02 13 43.01	7200	2016	Uniform Survey Mask
c16_24	10 00 49.014	+02 27 42.63	7200	2016	Uniform Survey Mask
c16_20	10 00 15.809	+02 28 04.78	7200	2016	Uniform Survey Mask
c16_22	10 00 32.398	+02 27 42.96	7200	2016	Uniform Survey Mask
c16_18	09 59 57.717	+02 27 32.81	9000	2016	Uniform Survey Mask
c17_27s	10 01 04.866	+02 13 39.53	10200	2017	Uniform Survey Mask
c17_29	10 01 06.761	+02 27 52.92	7200	2017	Uniform Survey Mask
c17_28s	10 01 07.846	+02 20 47.44	7200	2017	Uniform Survey Mask
c17_62	10 01 23.139	+02 27 33.91	12600	2017	Uniform Survey Mask
c17_61L	10 01 25.656	+02 21 00.15	12600	2017	Uniform Survey Mask
c17_60L	10 01 24.926	+02 13 42.49	9000	2017	Uniform Survey Mask
pc22L	10 00 30.622	+02 27 53.81	10800	2017	Targeted at $z \sim 2.5$ Cluster/Protocluster
sp18	10 00 16.563	+02 26 51.88	11100	2017	Designed to plug sightline gap
sp15l	09 59 52.268	+02 20 35.06	8700	2017	Designed to plug sightline gap

Notes.
[a] Mask name suffixes correspond roughly to field numbers shown in Figure 2.
[b] Slitmask pointing center.

Table 2
CLAMATO Data Release 1 Source Catalog

ID#	α (J2000)[a]	δ (J2000)[a]	g-mag[a]	$z_{\rm photo}$ [b]	$z_{\rm spec}$	Conf[c]	Type	$t_{\rm exp}$ (s)	Tomo[d]	S/N$_{\rm Ly\alpha1}$[e]	S/N$_{\rm Ly\alpha2}$ [f]	S/N$_{\rm Ly\alpha3}$[g]
00762	10 01 00.905	+02 17 27.96	24.21	1.11	2.465	2	GAL	7200	N	⋯	⋯	⋯
00765	10 01 00.297	+02 17 02.58	24.64	2.93	2.958	4	GAL	7200	Y	⋯	⋯	2.5
00767	10 01 14.934	+02 16 45.23	24.73	0.21	2.578	3	GAL	12600	Y	3.1	3.2	3.0
00771	10 01 06.870	+02 16 23.38	24.70	2.58	2.530	3	GAL	7200	Y	1.6	1.9	2.0
00780	10 01 14.359	+02 15 15.84	24.28	0.08	0.082	2	GAL	7200	N	⋯	⋯	⋯
00783	10 01 07.412	+02 14 58.31	24.27	2.59	2.579	4	GAL	10200	Y	4.1	4.5	4.7
00784	10 01 15.952	+02 14 48.41	22.02	2.47	2.494	4	QSO	9000	Y	11.5	13.1	22.1
00785	10 01 05.138	+02 14 41.21	24.51	2.44	2.506	4	GAL	10200	Y	2.1	2.5	2.8
00787	10 01 21.083	+02 14 16.48	24.41	2.62	2.491	3	GAL	9000	N	0.8	1.0	1.1
00788	10 01 33.860	+02 14 25.19	24.24	2.62	2.738	3	GAL	9000	Y	⋯	1.6	1.8

Notes.
[a] Source positions and magnitudes from Capak et al. (2007).
[b] Photometric redshift estimate; see the text for details.
[c] Redshift confidence grade, similar to that described in Lilly et al. (2007), but without fractional grades.
[d] Usage in Lyα forest tomographic reconstruction.
[e] Median per-pixel spectral continuum-to-noise ratio within the $2.05 < z_\alpha < 2.15$ Lyα forest.
[f] Median per-pixel spectral continuum-to-noise ratio within the $2.15 < z_\alpha < 2.35$ Lyα forest.
[g] Median per-pixel spectral continuum-to-noise ratio within the $2.35 < z_\alpha < 2.55$ Lyα forest.

(This table is available in its entirety in machine-readable form.)

determine their identity and redshift. For each spectrum, we assigned a confidence ranking of 0–4, where 0 implies no attempt at an identification (usually due to corrupted spectra or little/non-existent source flux), 1 is a guess, 2 is a low-confidence redshift, 3 denotes a reasonable confidence, while 4 is a high-confidence redshift derived from multiple spectral features. Out of the 437 reduced spectra, 289 spectra had confident identifications ($\geqslant$3 confidence rating), of which 277 were at redshifts $z > 2$ (Figure 4). These high-redshift sources can be further classified into 262 galaxies (95%) and 15 broad-line quasars (5%). Our main rationale for classifying a source as either a galaxy or quasar is to determine their continuum-fitting method; therefore we classified any source that showed intrinsic absorption lines at rest-frame $\lambda > 1216$ Å as a galaxy even if it shows a broad Lyα emission line indicative of AGN activity. Table 2 tabulates our full catalog of extracted sources, while examples of the high-redshift spectra are shown in Figure 5. The g- and r-magnitude (AB) distributions of

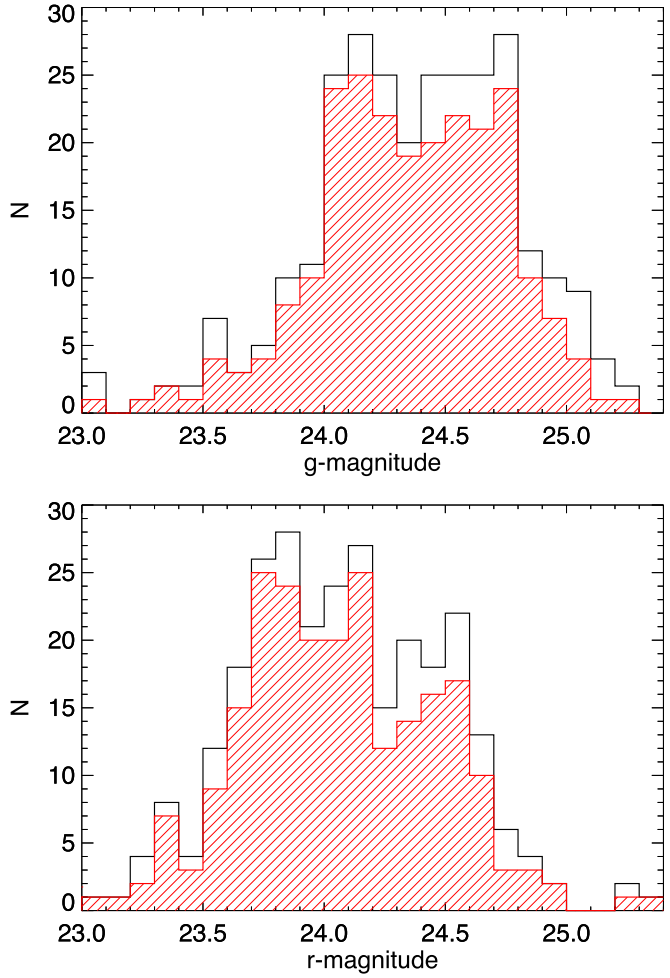

Figure 3. Magnitude distribution of CLAMATO objects with high-confidence (>3) redshift identifications, showing *g*-magnitude in the top panel and *r*-magnitude in the bottom panel. In both cases, the red histogram indicates objects that were subsequently used as background sources for the Lyα forest tomographic reconstruction. Small numbers of bright (<23rd magnitude) sources have been omitted in these axes.

high-confidence spectra are shown in Figure 3. The median magnitudes of all the high-confidence spectra, regardless of redshift, are $\langle g \rangle = 24.38$ and $\langle r \rangle = 24.03$, respectively. As we shall discuss later (Section 4), we will be quite aggressive in selecting background sources for Lyα forest reconstruction, therefore the median magnitudes of the final background sightline sample are only slightly brighter than this: $\langle g \rangle = 24.34$ and $\langle r \rangle = 24.02$.

The relatively low rate (65%) of confidently identified objects relative to the extracted spectra is because we filled any spare slits in our slitmasks with faint low-priority targets, which often resulted in spectra too noisy to be identified with confidence. However, of the spectra that did indeed get identified at high confidence, the yield of high-redshift ($z > 2$) objects is excellent (96%), reflecting our strategy of retargeting spectroscopic catalogs and the high quality of the photometric redshifts of those that had no prior spectroscopic redshifts.

For $z > 2$ LBGs, redshifts estimated from rest-frame-UV spectral features are known to have offsets from the "true" systemic redshifts as determined from rest-frame optical nebular emission lines (Steidel et al. 2010; Rakic et al. 2011). For CLAMATO, the redshift estimation of the spectra is intended to achieve two purposes: selection of the foreground Lyα forest absorption from the spectral region between the intrinsic Lyα and Lyβ wavelengths of the background source, and masking of the small number of intrinsic absorption lines within the Lyα forest. The selection of the Lyα forest pixels is relatively insensitive to the precise systemic redshift of the background source, but the masking of the intrinsic absorption lines is carried out with narrow spectral ranges. We therefore choose to estimate the source redshift, wherever possible, based on the rest-frame $\lambda > 1216$ Å absorption lines, since this allows the best masking of the absorption lines within the LBG forest.

The estimated redshifts for all 437 sources are provided in the online version of Table 2, including low-confidence objects. We have also made all the reduced spectra available for download; see Appendix A for details.

4. Tomographic Reconstruction

Prior to Lyα forest analysis, we first estimated the spectral signal-to-noise within the Lyα forest of the background sources at $z > 2$. To be more specific, we evaluated the "continuum-to-noise ratio" (CNR), i.e., the signal-to-noise ratio relative to a rough initial estimate of the background source intrinsic continuum, C. For the LBGs, this was done as a simple power-law extrapolation from the rest-frame $\lambda > 1216$ Å portion of the spectrum, while for the quasars we fitted principal components to the $\lambda > 1216$ Å spectrum, using templates from Pâris et al. (2011). Note that this initial continuum for the signal-to-noise estimation is different from that used to actually extract the Lyα forest (Equation (1), below), since this is much faster than the more careful mean-flux regulation used in Equation (1).

We evaluated the CNR of the Lyα forest pixels in each spectrum over three absorption redshift ranges: $2.05 < z_\alpha < 2.15$, $2.15 < z_\alpha < 2.35$, and $2.35 < z_\alpha < 2.55$. Any high-redshift spectrum with confidence $\geqslant 3$ that has $\langle \mathrm{CNR} \rangle \geqslant 1.2$ over either Lyα forest absorption redshift range was deemed useful for tomographic reconstruction. This is an aggressive choice that incorporates nearly every background object with a confident redshift estimate (Figure 4), leaving out only objects that were identified primarily through a Lyα emission line and therefore have negligible continua. We believe this is a reasonable approach because our Wiener-filtering reconstruction algorithm has noise-weighting, and Lee et al. (2014a) also argued for such an approach in the $\langle d_\perp \rangle \gtrsim 1.5\ h^{-1}$ Mpc shot-noise-dominated regime that CLAMATO is in.

These positions of the sightlines on the sky are shown in Figure 6. Note that this is a selection of Lyα forest sightlines specifically probing the $2.05 < z_\alpha < 2.55$ Lyα forest where we will carry out the tomographic reconstruction, and does not encompass all possible Lyα forest pixels in our data set; some of our other pixel-based analyses may make use of different selection criteria in position, redshift, and signal-to-noise than here.

There are 240 spectra within the redshift range $2.165 < z_{\mathrm{spec}} < 3.034$ (see Figure 4) that fulfilled both signal-to-noise and redshift criteria to contribute to the tomographic reconstruction of the foreground Lyα forest within at least part of the redshift range $2.05 < z_\alpha < 2.55$. The distribution of estimated Lyα forest signal-to-noise is shown in Figure 7 at several redshifts within our volume. A

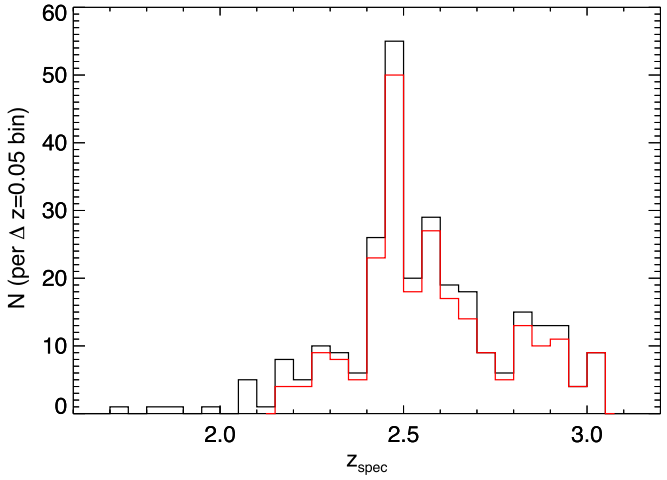

Figure 4. Redshift distribution of well-identified (⩾3 confidence rating) spectra in the current CLAMATO data release, shown as the black histogram with redshift bins of $\Delta(z) = 0.05$. The red histogram indicates background sources that were actually used to tomographicaly reconstruct the foreground Lyα forest at $2.05 < z_\alpha < 2.55$. These plot axes leave out 8 objects at $z < 1.6$ and 1 object at $z > 3.2$.

power law with an index of −2.7, which was adopted by Krolewski et al. (2017) and Krolewski et al. (2018), is a reasonable match for this distribution. Based on the positions of these sightlines, we defined a transverse footprint for the tomographic reconstruction. This spans a comoving region of $26\farcm6 \times 21\farcm3$ in the R.A. and declination dimensions, respectively (Figure 6); the center of this footprint is at $10^{\rm h}00^{\rm m}41\fs23$, $+02°19'38\farcs78$ (J2000). This is equivalent to a transverse comoving scale of $30\,h^{-1}$ Mpc × $24\,h^{-1}$ Mpc at $\langle z\rangle = 2.30$. The overall projected area density of all the sightlines that fall within the map footprint[29] is $N_{\rm los} = 1455\,{\rm deg}^{-2}$. However, due to the finite path length of Lyα forest probed by each background spectrum, the differential sightline density, $n_{\rm los}(z) = dN_{\rm los}/dz$, at any given redshift within the volume is somewhat lower than this. Averaged over the redshift range of the map, the mean sightline density is $\langle n_{\rm los}\rangle = 866\,{\rm deg}^{-2}$, equivalent to a mean sightline separation of $\langle d_\perp\rangle = 2.35\,h^{-1}$ Mpc. At the low- and high-redshift ends of the map volume ($z = [2.05, 2.55]$), the effective sightline density is $n_{\rm los} = [673, 451]\,{\rm deg}^{-2}$, equivalent to average transverse comoving separations of $\langle d_\perp\rangle = [2.61, 3.18]\,h^{-1}$ Mpc between sightlines (see Figure 8). The effective sightline density increases toward the middle of the map redshift range, to a peak density of $1099\,{\rm deg}^{-2}$ at $z_\alpha = 2.32$, near the mean redshift,. This is equivalent to $\langle d_\perp\rangle = 2.04\,h^{-1}$ Mpc comoving transverse separation. Note that these sightline densities are not uniformly distributed throughout the map footprint, due to shot noise as well as some background source clustering from the known galaxy overdensities at $z \sim 2.5$.

In comparison, the BOSS sightline density—which hitherto had the best 3D sampling of the Lyα forest—is often quoted as $16\,{\rm deg}^{-2}$ (Lee et al. 2013), but this is in fact the projected sightline density over all redshifts; the effective sightline density (which gives the transverse sightline separation at a given redshift) for BOSS peaks at $9\,{\rm deg}^{-2}$ at $z_\alpha = 2.3$.

[29] For this calculation, we ignore sightlines that fall outside the map boundary (Figure 6), although they will nonetheless contribute to the tomographic reconstruction.

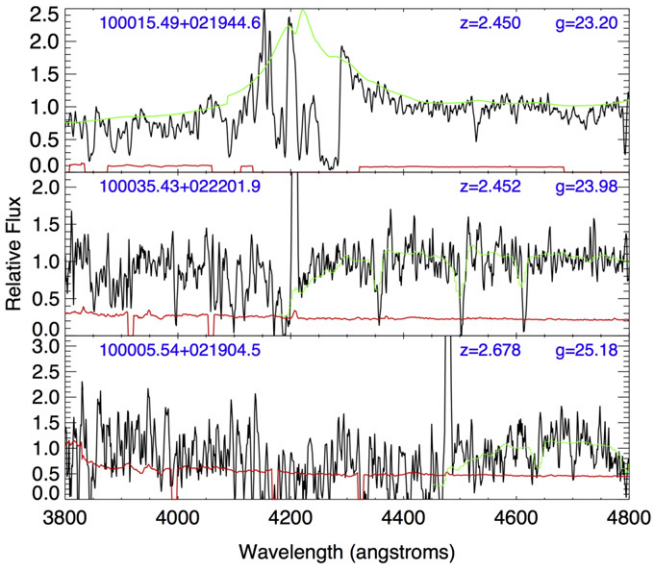

Figure 5. Examples of the reduced high-redshift spectra from our data set. The object at the top is a quasar, while the others are LBGs with Lyα emission. For clarity, the spectra have been smoothed with a 3-pixel top-hat filter. The galaxy at the bottom is among our faintest objects, and has marginally sufficient signal-to-noise in the Lyα forest to contribute to our tomographic reconstruction thanks to an above-average 6 hr of exposure over multiple slitmasks.

CLAMATO therefore represents an increase by two orders of magnitude in the sightline density probing the Lyα forest, albeit over a much more limited area.

For the spectra that we want to analyze, we divide the observed spectral flux density, f, by the estimated continuum, C, and the assumed mean Lyα forest transmitted flux, $\langle F\rangle(z)$, at that redshift, to obtain the Lyα forest fluctuation at each pixel:

$$\delta_F = \frac{f}{C\,\langle F\rangle(z)} - 1. \quad (1)$$

We adopt the Faucher-Giguère et al. (2008) values for $\langle F\rangle(z)$.

The intrinsic continua, C, of the sources is estimated differently depending on whether they are galaxies or quasars. For the quasars, we apply PCA-based mean-flux regulation (MF-PCA; e.g., Lee et al. 2012, 2013). Each spectrum is fitted with a continuum template to obtain the correct shape for the intrinsic emission lines, which is further fitted with a linear function within the Lyα forest region such that it yields a mean absorption consistent with Faucher-Giguère et al. (2008). Since the integrated forest variance over each $\sim$400 h^{-1} Mpc sightline is equivalent to only $\sim$2% rms (e.g., Tytler et al. 2004), this technique allows automated continuum-fitting with <10% rms errors even with noisy spectra. This technique was applied to the rest-frame 1041 Å $< \lambda <$ 1185 Å Lyα forest region of the quasar spectra using templates from Pâris et al. (2011), masking intrinsic broad absorption where necessary.

A similar process is applied on the galaxies, albeit assuming a fixed continuum template from Berry et al. (2012) and adopting a more generous Lyα forest range (1040 Å $< \lambda <$ 1195 Å). We also mask ±7.5 Å (observed frame) around possible intrinsic absorption at rest-frame N II λ1084, N I λ1134, C III λ1176, and Si II $\lambda\lambda$1190, 1193. We estimate that the continuum errors are approximately $\sim$10% rms for the noisiest spectra (S/N $\sim$ 2 per pixel) and improving to $\sim$4% rms for S/N $\sim$ 10 spectra (Lee et al. 2012).

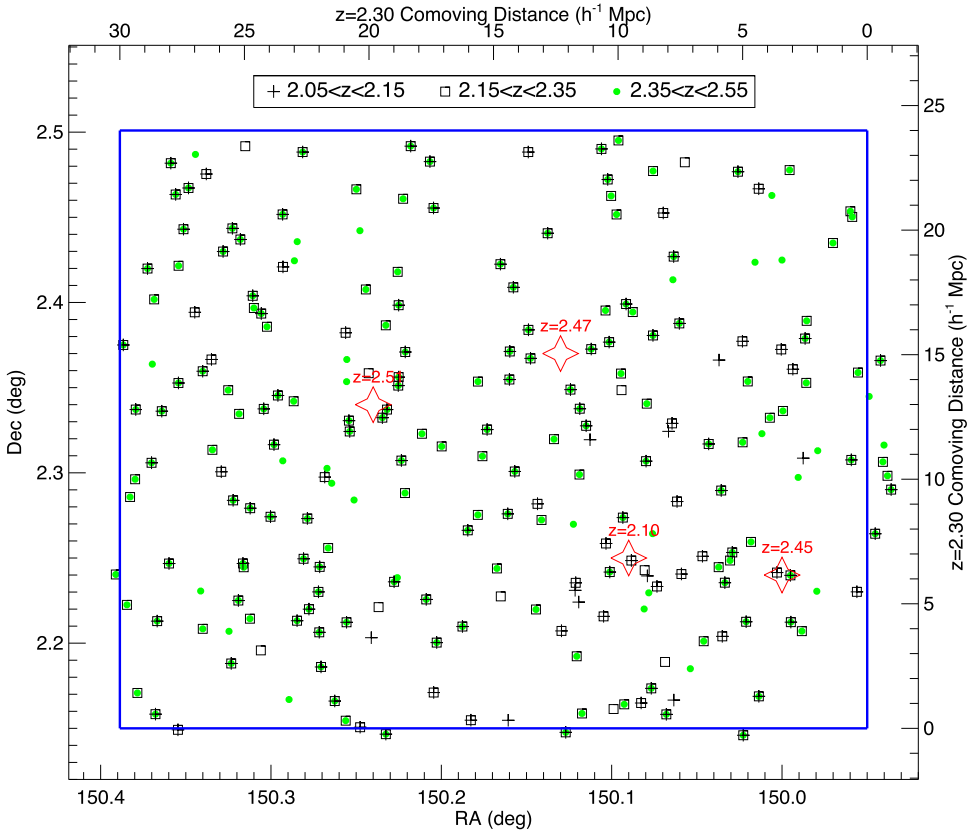

Figure 6. Angular position of the Lyα forest sightlines used to tomographically reconstruct the Lyα forest at $2.05 < z < 2.55$. The different symbols denote coverage over different redshift ranges. Some background sources have the correct redshift to cover large ranges of our targeted foreground redshift range and are therefore indicated by multiple symbols. We have also marked with red diamonds the angular position of several known overdensities, at $z = 2.10$ (Spitler et al. 2012; Nanayakkara et al. 2016), $z = 2.44$ (Chiang et al. 2015; Diener et al. 2015), $z = 2.47$ (Casey et al. 2015), and $z = 2.51$ (Wang et al. 2016). The top and right axes denote the transverse comoving distances in the coordinates of our tomographic map grid.

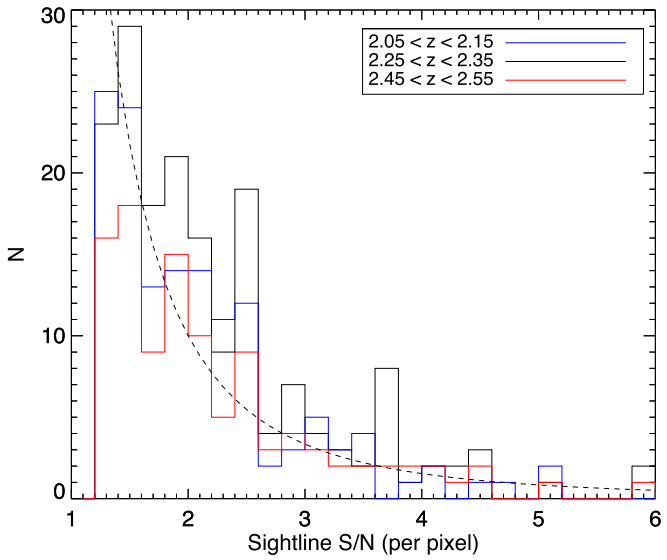

Figure 7. Distribution of the median sightline signal-to-noise within the Lyα forest, evaluated at several redshift bins of our map volume. A small number of higher signal-to-noise sightlines have been left out by these plot axes. The dashed curve is a power law with an index of -2.7, which is a reasonable approximation for our signal-to-noise distribution.

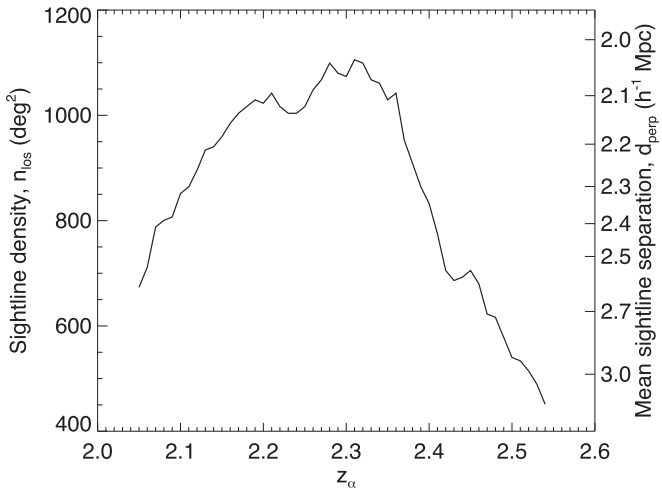

Figure 8. Effective area density of Lyα forest sightlines over the redshift range of the CLAMATO tomographic reconstruction. The right axis labels the equivalent mean separation between sightlines, $\langle d_\perp \rangle$. The peak sightline density is 1099 deg^{-2} at $z_\alpha = 2.32$, corresponding to $\langle d_\perp \rangle = 2.04\ h^{-1}$ Mpc.

The δ_F pixel values, as well as the associated noise uncertainty, σ_N, from the pipeline, constitute the input for the tomographic reconstruction. We have made these extracted δ_F and σ_N pixel data publicly available; see Appendix A for details.

The next step for the reconstruction is to define the three-dimensional comoving output grid for the map. We choose an area spanning $26\farcm6 \times 21\farcm3$ in the longitudinal and latitudinal dimensions, respectively (Figure 6), and spanning a redshift range of $2.05 < z < 2.55$. The angular footprint of this grid is

3.5× larger than that in Lee et al. (2016), while we have also extended the redshift range by 67% from $2.20 < z_\alpha < 2.50$ to $2.05 < z_\alpha < 2.55$. The extension to lower redshifts was because we realized that that the sightline density was higher at lower redshifts than originally anticipated (Figure 8), while we also extended to slightly higher redshifts in order to investigate the Wang et al. (2016) galaxy cluster at $z = 2.51$ despite the falling sightline density.

We adopt the simplification of a fixed Hubble parameter, $H(z)$, throughout our map volume evaluated at the mean redshift, $\langle z \rangle = 2.30$. This means that the differential comoving distance, $d\chi/dz$, is constant throughout our map, such that a redshift segment of length δz is equivalent to the same comoving distance $\delta\chi$ everywhere in our grid. The $26\farcm6 \times 21\farcm3$ transverse footprint of the output grid therefore translates to a fixed transverse comoving scale of $30\ h^{-1}$ Mpc × $24\ h^{-1}$ Mpc at all redshifts in our map. These approximations mean that we will have a smoothing kernel (see below) that actually varies in size by several percent between the nearest and farthest ends of the map, but this simplification dramatically eases our mapmaking. We also tested performing the Wiener filtering over the pixel data transformed to $[x, y, z]$ comoving coordinates using the evolving $H(z)$ over our redshift range, such that the sightline pixels appeared to flare outward relative to the comoving grid. The resulting map was found to have a negligible effect on the cosmic void analysis of Krolewski et al. (2018), but breaks the one-to-one correspondence between (R.A., decl.) and the transverse $[x, y]$ coordinates of the comoving grid. For our fiducial map, we therefore decide to use the approximation of a constant $H(z)$ over our map in order to preserve the one-to-one relationship between (R.A., decl.) and transverse $[x, y]$, which facilitates comparisons with coeval galaxy positions. More detailed cosmological analyses would require the correct $H(z)$ to be adopted, but those would tend to directly use the pixel data rather than going through the tomographic map reconstruction.

With this approximation, we thus define an output grid of $60 \times 48 \times 876$ cells each $0.5\ h^{-1}$ Mpc on a side. This cell size allows an adequate sampling of our tomographic reconstruction, which has an effective smoothing scale of ∼2–3 h^{-1} Mpc. The overall comoving volume covered by the output grid is thus $3.15 \times 10^5\ h^{-3}$ Mpc^3. This is 5.4× larger in comoving volume than the map described in Lee et al. (2016).

For the mapmaking, we use a Wiener filtering scheme for reconstructing the sightlines (although see Cisewski et al. 2014 for an alternative method). The basic algorithm is described in Pichon et al. (2001) and Caucci et al. (2008), but we use an implementation[30] developed by Stark et al. (2015a). This solves for the reconstructed Lyα forest flux field:

$$\delta_F^{\rm rec} = \boldsymbol{C}_{\rm MD} \cdot (\boldsymbol{C}_{\rm DD} + \boldsymbol{N})^{-1} \cdot \delta_F, \tag{2}$$

where $\boldsymbol{C}_{\rm DD} + \boldsymbol{N}$ and $\boldsymbol{C}_{\rm MD}$ are the data–data and map–data covariances, respectively. This algorithm uses preconditioned conjugate gradient technique to solve the matrix inversion and matrix multiplication steps of reconstruction. We assumed a diagonal form for the noise covariance matrix $\boldsymbol{N} \equiv N_{ii} = \sigma_{N,i}^2$, such that there were only diagonal elements populated by the pixel variances $\sigma_{N,i}^2$. However, there is a small number of spectra, primarily from bright quasars, with signal-to-noise ratios >10× larger than the average, that could dominate the reconstruction due to the noise-weighting of the Wiener filter. We therefore introduced a noise floor of $\sigma_{N,i} \geqslant 0.2$ to the noise vector to allow a more uniform contribution from all sightlines.

We also assumed a Gaussian covariance between any two points r_1 and r_2, such that $\boldsymbol{C}_{\rm DD} = \boldsymbol{C}_{\rm MD} = \boldsymbol{C}(\boldsymbol{r}_1, \boldsymbol{r}_2)$ and

$$\boldsymbol{C}(\boldsymbol{r}_1, \boldsymbol{r}_2) = \sigma_F^2 \exp\left[-\frac{(\Delta r_\parallel)^2}{2L_\parallel^2}\right] \exp\left[-\frac{(\Delta r_\perp)^2}{2L_\perp^2}\right], \tag{3}$$

where $\Delta r_\parallel$ and $\Delta r_\perp$ are the distance between $\boldsymbol{r}_1$ and $\boldsymbol{r}_2$ along, and transverse to the line of sight, respectively. This Gaussian form was found by Stark et al. (2015b) to be a reasonable approximation to the true correlation function of the Lyα forest. We adopt transverse and line-of-sight correlation lengths of $L_\perp = 2.5\ h^{-1}$ Mpc and $L_\parallel = 2.0\ h^{-1}$ Mpc, respectively, as well as a normalization of $\sigma_F^2 = 0.05$. These forms of covariance and parameters were determined by Stark et al. (2015b) to be approximately optimal for our data. Intuitively, $L_\perp$ can be thought of as set by our average sightline separation, i.e., $L_\perp \approx \langle d_\perp \rangle$, while $L_\parallel^2 \approx L_\perp^2 - \sigma_{\rm lsf}^2$, i.e. it takes into account the spectral smoothing by the spectrograph, $\sigma_{\rm lsf}$, to match $L_\perp$ in the line-of-sight dimension and thus provide an isotropic smoothing kernel.

We carried out the Wiener reconstruction of the map data from the 64332 input pixels with the aforementioned parameters using the Stark et al. (2015a) algorithm, with a stopping tolerance of 10^{-3} for the preconditioned conjugation gradient solver. This required a runtime of approximately 1000s using a single core of a Apple MacBook Pro laptop with 2.9 GHz Intel Core i5 processors and 16 GB of RAM.

In addition to the map itself, we have also computed the map variance associated with the Wiener reconstruction:

$$\mathrm{Var}(\delta_F^{\rm rec}) = \boldsymbol{C}_{\rm MD} \cdot (\boldsymbol{C}_{\rm DD} + \boldsymbol{N})^{-1} \boldsymbol{C}_{\rm DM}, \tag{4}$$

where $\boldsymbol{C}_{\rm DM} \equiv \boldsymbol{C}_{\rm MD}^{\rm T}$. The variances were far more computationally intensive to calculate than the map itself (by a factor of $N_{\rm pix}$), but will allow analyses to take account of reconstruction uncertainties. This estimate incorporates all sources of variances in the map, including pixel noise, finite skewer sampling, and intrinsic variance of the Lyα forest. We will further discuss these in Section 6.

The resulting map and standard deviations are publicly available for download as a binary file; see Appendix A for details.

5. Results

In Figure 9 we show a slice visualization of the resulting tomographic map, where we have divided the three-dimensional volume into projected slices over the longitudinal (i.e., R.A.) direction with thicknesses of $2\ h^{-1}$ Mpc. The x-axis of each slice therefore denotes the redshift or line-of-sight dimension, while the y-axes are along the declination or latitudinal dimension in the plane of the sky. For clarity, we have found it useful to further smooth the map with a Gaussian kernel, in this case with standard deviation $R = 2\ h^{-1}$ Mpc. For comparison, we have also overplotted the positions of 552 known coeval spectroscopic redshifts that overlap our map volume, which are primarily from zCOSMOS-Deep (Lilly et al. 2007) and VUDS (Le Fèvre et al. 2015), but also from publicly released redshifts such as MOSDEF (Kriek

[30] https://github.com/caseywstark/dachshund

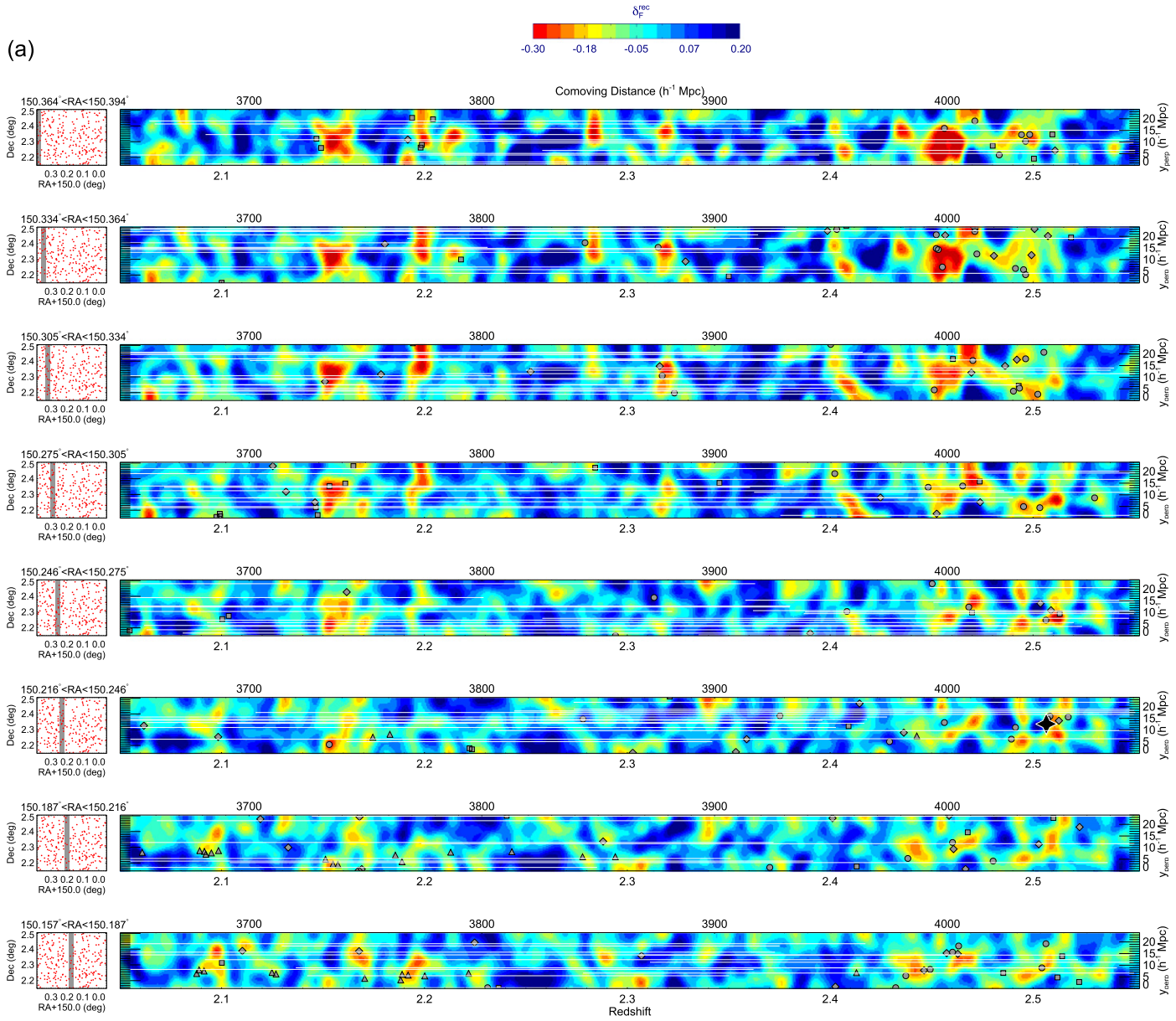

Figure 9. Wiener-filtered tomographic reconstructions of the Lyα forest absorption field, $\delta_F^{\rm rec}$, at $2.05 < z_\alpha < 2.55$ from the current CLAMATO data (color map), shown after smoothing with an isotropic $R = 2\,h^{-1}$ Mpc Gaussian kernel. Each color panel shows the absorption projected over a $2\,h^{-1}$ Mpc R.A. slice, the position of which is denoted by the shaded region in the subpanels to the left that also show the sightline positions on the sky as red dots. The color convention for the absorption is such that red denotes overdensities, while blue denotes underdensities. White horizontal lines denote the sightline coverage, while symbols mark the location of known foreground galaxy redshifts: downward triangles for MOSDEF, upward triangles for ZFIRE, squares for VUDS, diamonds for zCOSMOS-Deep, and circles for CLAMATO. The large black stars indicate the reported central positions of the galaxy overdensities at $z = [2.10, 2.44, 2.47, 2.51]$. This sequence is continued in Figure 9(b).

et al. 2015) and ZFIRE (Nanayakkara et al. 2016). We also included the positions of our own CLAMATO galaxies that fell within the foreground map volume. For the galaxies with spectroscopic redshifts from more than one survey, we used the redshift estimates in the following order of descending priority: MOSDEF, ZFIRE, CLAMATO, VUDS, then zCOSMOS-Deep. In addition to the two-dimensional visualization, we have also created a video visualization (Figure 10), as well as a manipulable interactive figure for the online journal (Figure 11); more details on these 3D visualizations are given in Appendix B.

While there are multiple science analyses in preparation based on the CLAMATO data presented in this paper, here we qualitatively discuss the more notable features apparent in the tomographic Lyα forest absorption map described in the previous section.

5.1. Large-scale Structure Features

In all these visualizations, the IGM absorption and the coeval galaxies generally appear to trace the same structures. However, the foreground galaxy redshifts are incomplete across our volume, and several of the spectroscopic surveys (i.e., MOSFIRE and ZFIRE) target only a limited sub-field within the central portion of the CLAMATO footprint (see Figure 1). It would therefore be challenging to construct a uniform density map from the galaxy redshifts, whereas the

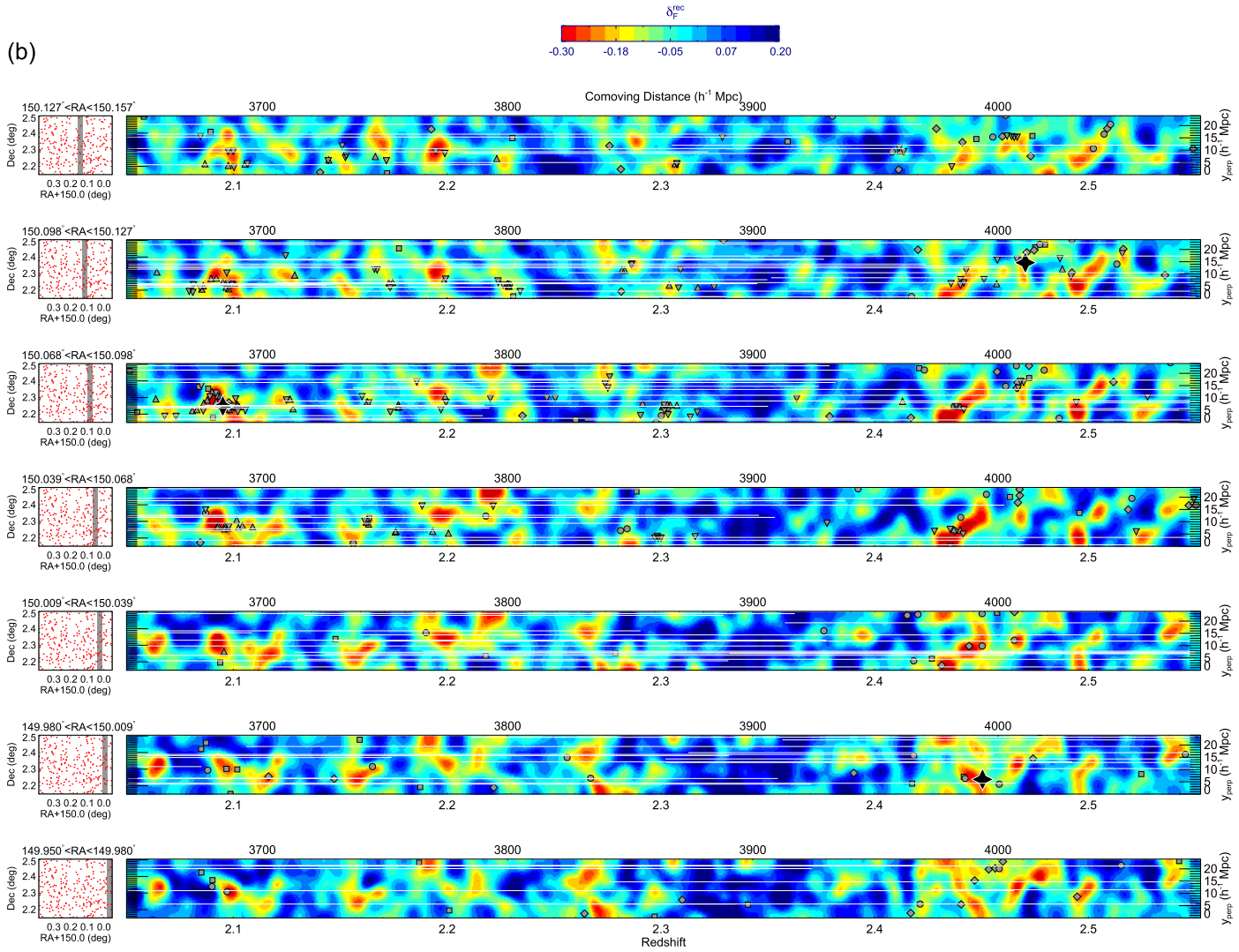

Figure 9. (Continued.)

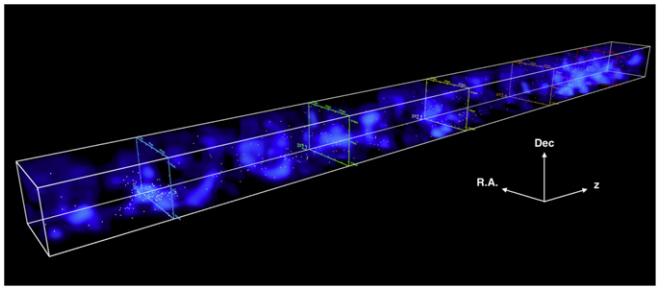

Figure 10. Still image from our 3D video visualization of the CLAMATO reconstructed absorption map (smoothed with a $R = 2\,h^{-1}$ Mpc Gaussian kernel), where the absorption is indicated by the blue transparency. Foreground galaxy redshift positions are denoted by the yellow dots, while the triad (not present in the video) indicates the directions of increasing R.A., declination, and redshift. Alternatively, the YouTube version (https://youtu.be/QGtXi7P4u4g) offers a virtual-reality option when viewed with a smartphone and a headset compatible with Google Cardboard.

(An animation of this figure is available.)

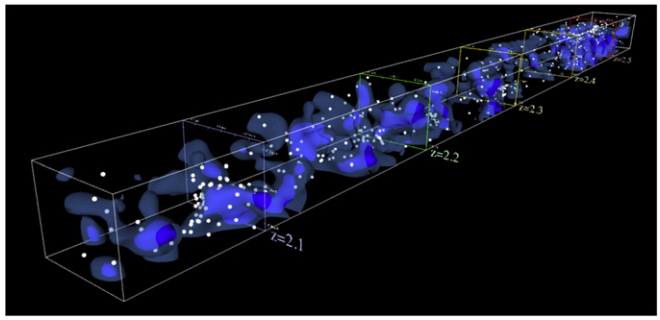

Figure 11. Three-dimensional rendering of the CLAMATO tomographic map, showing two isodensity contours at $\delta_F^{rec} = -0.08$ and $\delta_F^{rec} = -0.18$, along with coeval galaxy positions shown as dots. This figure is available online as an interactive figure—it requires a load-time of several minutes. By left-clicking and moving the mouse, the viewpoint can be rotated, while the right mouse button or scroll wheel can be used to zoom in or out; double left-clicking at any point in the map focuses the viewpoint there. The buttons labeled "Isosurface: $-0.''08$ and "$-0.''18$ toggle the respective isodensity surfaces on and off. The "Reset View" button restores the figure to its default state and perspective.

tomographic map delivers a more detailed view of large-scale structure in that volume. In upcoming papers, we will investigate the relationship between galaxy properties and their density environment, assuming that the Lyα forest absorption traces large-scale structure. There will be alternative analyses using different formalisms: a direct comparison of

galaxy positions with the local IGM absorption, and a pixel-level cross-correlation analysis analogous to those carried out in BOSS for quasars and damped Lyα absorbers (Font-Ribera et al. 2012, 2013). In both cases, we will aim to carry out the investigations as a function of galaxy properties fitted from their spectral energy distributions. A recent study (Sorini et al. 2017) has also argued that the precise shape of the galaxy-forest cross-correlation on $\sim 1\ h^{-1}$ Mpc scales could be used to place constraints on galaxy feedback, which will make feedback models another parameter space we could investigate.

With reference to the galaxy redshifts alone, an apparent lack of galaxies at any point in space in these visualizations do not necessary imply a true absence of galaxies due to the incompleteness of the galaxy surveys. But in the IGM map, we clearly see large coherent underdensities, with a notably striking underdensity at $z \approx 2.35$ appearing to extend $>10\ h^{-1}$ Mpc along both the transverse and line-of-sight dimensions. These underdensities also appear to be devoid of galaxies and therefore are likely to be true cosmic voids. A detailed analysis of the cosmic voids in the CLAMATO map, which are by far the most distant such objects ever found, is presented in a companion paper (Krolewski et al. 2018).

Conversely, we see excess absorption corresponding to multiple galaxy overdensities that have been identified through other methods. In particular, we clearly see the extended Lyα absorption signature from the $z \approx 2.5$ overdensity comprised of the $z = 2.44$ protocluster (Chiang et al. 2015; Diener et al. 2015), $z = 2.47$ protocluster (Casey et al. 2015), and X-ray detected $z = 2.51$ cluster (Wang et al. 2016). In the 3D visualizations (Figures 10 and 11), we see that these structures appear to form a giant interconnected structure extending roughly from $2.44 < z < 2.52$ with a complex topology. Another known overdensity seen in our map is the $z = 2.095$ galaxy protocluster initially identified through the ZFOURGE medium-band photometric redshift survey (Spitler et al. 2012) and subsequently confirmed with NIR spectroscopy (Nanayakkara et al. 2016). In an upcoming paper we will analyze the properties of these overdensities in conjunction with large-volume hydrodynamical simulations, although further CLAMATO data will be required in order to fully map out the extent of these overdensities since they overfill our current map boundaries. In particular, we are interested in the fate of the $z = 2.44$–2.51 system of overdensities: Wang et al. (2016) have argued that the $z = 2.51$ overdensity, in itself, might collapse into a $2 \times 10^{15}\ M_{\odot}$ galaxy cluster at late times, i.e., it might be fated to become one of the most massive clusters in the known universe. With the detailed large-scale structure information from IGM tomography, we aim to carry out a detailed investigation into the evolution of these structures, especially using constrained realization techniques (e.g., Wang et al. 2014; Jasche et al. 2015).

6. Quality Assessment

6.1. Wiener-based Map Variance

First, the variances estimated from the Wiener filtering algorithm (Equation (4)) provide the most obvious approach to quantify the fidelity of the map. We find that mean value for the estimated variance is $\langle \mathrm{Var}(\delta_F^{\mathrm{rec}}) \rangle = 0.0219$ within the $L = 0.5\ h^{-1}$ Mpc volume elements ("voxels") in our reconstruction. This variance includes contributions from the intrinsic variance of the Lyα forest, as well as pixel noise and finite sightline sampling. In order to estimate the uncertainties caused by noise and sampling variance contributions, we therefore need to subtract the intrinsic variance. We do this using the simulated fluxes from the $L = 256\ h^{-1}$ Mpc N-body simulations described in Stark et al. (2015a, 2015b), which we binned to the same voxel size and smoothed with a Gaussian kernel of the same size as applied to the real map (Equation (3)). The intrinsic Lyα forest variance estimated from the simulation is $\mathrm{Var}^{\mathrm{intr}}(\delta_F) = 0.00654$.

We can thus proceed to define the global signal-to-noise ratio as

$$\mathrm{S}/\mathrm{N}^{\mathrm{wiener}} \equiv \sqrt{\frac{\mathrm{Var}^{\mathrm{intr}}(\delta_F)}{\langle \mathrm{Var}(\delta_F^{\mathrm{rec}}) \rangle - \mathrm{Var}^{\mathrm{intr}}(\delta_F)}}, \tag{5}$$

i.e., the square-rooted ratio of the intrinsic variance of the Lyα forest (the signal) compared with the variance contributions from the pixel noise and finite sightline sampling. For our current map, we find $\mathrm{S}/\mathrm{N}^{\mathrm{wiener}} \approx 0.65$ per individual $0.5\ h^{-1}$ Mpc voxel. Over larger scales used for most analyses, the signal-to-noise is commensurately improved as the square root of the number of pixels being averaged over. For example, over top-hat kernels of [2, 3, 4] h^{-1} Mpc, the signal-to-noise would on average be improved to $\mathrm{S}/\mathrm{N}^{\mathrm{wiener}} \approx [1.8, 3.4, 5.2]$, respectively.

6.2. Comparison with the Forecasts of Lee et al. (2014a)

In Lee et al. (2014a), we made predictions for the quality of IGM tomographic maps based on various observational scenarios. We now compare our actual data with the earlier forecasts. In Lee et al. (2014a), we defined the following quantity[31] based on the deviation of mock tomographic reconstructions with respect to the true underlying flux in the simulations:

$$S_{\epsilon} = \sqrt{\frac{\mathrm{Var}(\delta_F^{\mathrm{true}})}{\mathrm{Var}(\delta_F^{\mathrm{rec}} - \delta_F^{\mathrm{true}})}}, \tag{6}$$

where δ_F^{true} is the true Lyα forest flux field from the simulation and δ_F^{rec} is the tomographic reconstruction of mock data from the same volume. For this purpose, we use the aforementioned $L = 256\ h^{-1}$ Mpc N-body simulations. We first divide up the simulation volume into $32\ h^{-1}$ Mpc$\times$ $32\ h^{-1}$ Mpc $\times$ $256\ h^{-1}$ Mpc chunks to approximate the elongated CLAMATO survey geometry, randomly drawing Lyα forest absorption skewers with a mean sightline separation of $\langle d_{\perp} \rangle = 2.5\ h^{-1}$ Mpc, and then adding Gaussian random noise to each sightline's pixels, consistent with the signal-to-noise distribution of the CLAMATO sightlines. We also introduced a random continuum error to each sightline based on the sightline signal-to-noise: we assumed an inverse relationship between the signal-to-noise and continuum error, such that, e.g., a $\mathrm{S}/\mathrm{N} = 2$ sightline gets 12% continuum error, while a $\mathrm{S}/\mathrm{N} = 10$ sightline gets only a 3.5% continuum error (for more details, see Krolewski et al. 2018). The sightlines from each mock survey are then Wiener-reconstructed the same way as the CLAMATO data.

[31] This quantity was denoted as $\mathrm{S}/\mathrm{N}_{\epsilon}$ in Lee et al. (2014a), but here we rename it to avoid confusion with the quantity defined in Equation (5).

Following the prescription from Lee et al. (2014a), we then Gaussian-smooth both the true and reconstructed flux fields with a $R = 4\ h^{-1}$ Mpc kernel (i.e., a smoothing kernel 1.4 × the mean sightline separation) before calculating the simulation-estimated signal-to-noise. For CLAMATO, we find $S_\epsilon = 2.26$ after averaging over 64 mock survey volumes. This is a slightly conservative estimate since the $\langle d_\perp \rangle = 2.5\ h^{-1}$ Mpc sightline separation assumed in the mocks is sparser than the average $\langle d_\perp \rangle = 2.37\ h^{-1}$ Mpc over our entire map, but it is within the $S_\epsilon \sim 2$–2.5 range of what Lee et al. (2014a) considered a good reconstruction quality. We also cross-checked this with the analytic method for calculating S_ϵ (Equation (18) in Lee et al. 2014a), which takes as input the sightline signal-to-noise distribution. This calculation yields $S_\epsilon = 2.30$, which is in good agreement with the estimate from the mock reconstructions.[32] This suggests that the analytic formalism would be a useful tool for forecasting future IGM tomography surveys to provide signal-to-noise estimates relative to CLAMATO.

However, in retrospect we now find the forecasts from Lee et al. (2014a) to be optimistic compared to what we have been obtaining with CLAMATO. In particular, the forecasted area density of LBGs at fixed magnitude is considerably lower than what we observe. Lee et al. (2014a), for example, projected a sightline density of 660 deg^{-2} at a magnitude limit of $g \leqslant 24.2$, whereas we have the equivalent of 344 deg^{-2} at the same limit. This shortfall is apparent not just within the present CLAMATO data, but also when looking at all possible targets with the appropriate brightness and photometric redshifts across the full COSMOS field based on the Laigle et al. (2016) catalog. We believe this is a genuine discrepancy and attribute it to the likely combination of several factors: (i) a mismatch between the g filter assumed in Lee et al. (2014a) and the different filter set of Reddy et al. (2008), whose luminosity function was used to estimate sightline availability, (ii) uncertainties in the luminosity function, whose error bars are a factor of 2 or 3 at the bright end. Due to the steep slope at the bright end of the luminosity function, even small discrepancies could translate to large differences in number count.

The scaling of spectral signal-to-noise with exposure time in Lee et al. (2014a) was also found to be too optimistic. The older paper assumed, for example, that a 4 hr exposure with the VLT (equivalent to 2.6 hr on with the larger Keck telescope) would yield S/N = 4 per angstrom on a $g = 24.0$. We find, on the other hand, that a comparable exposure time yields only S/N ≈ 3 per angstrom (with a considerable scatter) on a similar source magnitude. This is most likely due to the fact that Lee et al. (2014a) assumed that the star-forming (and hence UV-emitting) regions of the background galaxies are point sources, whereas real LBGs are sufficiently extended as to increase the amount of sky background noise beyond that assumed by Lee et al. (2014a).

In the CLAMATO observations, we made up for these shortfalls by filling our slitmasks with targets even if they fall below our nominal survey limit, and then being aggressive in incorporating low-signal-to-noise spectra into our tomographic reconstruction. Lee et al. (2014a) calculated that adding more low-signal-to-noise spectra is a viable survey strategy to boost the tomographic map signal-to-noise in the $\langle d_\perp \rangle \gtrsim 1\ h^{-1}$ Mpc shot-noise-dominated scales that CLAMATO is probing. We have also reobserved many fields within our footprint, both to obtain additional integration times or with redesigned slitmasks, as new targeting information became available. Our sightline coverage is therefore more homogeneous than if we had pursued a single-pass strategy with fixed exposure time, and even then there are gaps in the footprint that we were not able to fill after 10 hr of integration (see Table 1).

We were also likely helped by the presence of the overdensities at $z \sim 2.44$–2.51, which provided additional sightlines for the $z_\alpha < 2.4$ map region in their foreground. We therefore expect our mean sightline separation to increase from the current $\langle d_\perp \rangle = 2.37\ h^{-1}$ Mpc as the survey footprint extends into the rest of the COSMOS field.

7. Conclusion

In this paper, we have described the first data release of the CLAMATO Survey, the first systematic attempt at implementing 3D Lyα forest reconstruction on several-megaparsec scales using high area densities (∼1000 deg^{-2}) of background LBG and quasar spectra.

With Keck I LRIS observations of 23 multi-object slitmasks over 0.157deg^2 in the COSMOS field, we obtained 293 spectra with confident redshifts, of which 240 were at the right redshift and had sufficient signal-to-noise to use as background sources probing the $2.05 < z_\alpha < 2.55$ Lyα forest. The average transverse separation between these sightlines is only $\langle d_\perp \rangle = 2.35\ h^{-1}$ Mpc. We used these spectra to create a three-dimensional tomographic map of the IGM absorption at these redshifts, which has comoving dimensions of $30\ h^{-1}$ Mpc × $24\ h^{-1}$ Mpc × $438\ h^{-1}$ Mpc. We have made

$$\simeq 3.15 \times 10^5\ h^{-3}\ \mathrm{Mpc}^3$$

all the catalogs, spectra, pixel data, and reconstructed maps publicly available (see Appendix A).

By eye, the CLAMATO absorption map appears to trace similar structures as the coeval galaxies with known spectroscopic redshifts within the COSMOS field, and also reveals large extended structures associated with several known galaxy overdensities in the field. There are also clear underdensities that are also devoid of galaxies and hence correspond to cosmic voids (Krolewski et al. 2018). Multiple science analyses are now ongoing on this data, including measuring the cross-correlation between the Lyα forest and coeval galaxies, studying galaxy properties as a function of IGM environment, and analysis of the protoclusters in the volume.

Over the next few years, we hope to expand the CLAMATO map to at least 0.5 deg^2, which will achieve a cosmological volume of $10^6\ h^{-3}$ Mpc^3. This will give full coverage of the large overdensities that we currently see in the map, and cover ∼1200 coeval galaxies, which would offer sufficient statistical power for comparative studies of their properties as a function of IGM environment. For cosmology, preliminary estimates suggest that the full CLAMATO survey will have comparable numbers of unique 3D Lyα forest pixel pairs at several-megaparsec separations as the 1D pixel pairs at similar scales used in the BOSS DR9 one-dimensional forest flux power spectrum measurement (Palanque-Delabrouille et al. 2013b). This could allow interesting complementary constraints on cosmological parameters such as the sum of neutrino masses and the curvature of the primordial density fluctuation power spectrum. Another interesting measurement that could be

[32] To assist in planning of future IGM tomography surveys, we have made the analytic code publicly available under an MIT license: https://github.com/kheegan/tomo_mapsn and archived Version 1 on Zenodo (Lee 2018).

attempted with the CLAMATO data is the weak-lensing of the Lyα forest (Croft et al. 2017), which uses the gravitational deflection of the $z \sim 2$–3 Lyα forest to probe the $z \sim 1$ matter field, which is at a higher redshift than is currently probed by galaxy cosmic shear weak lensing measurements. Based on the estimates from Metcalf et al. (2017), the 0.5 deg^2 CLAMATO survey should be able to detect Lyα forest weak lensing at $\sim 6\sigma$ confidence over a foreground redshift range of $\Delta z = 0.5$—this signal should be even stronger in cross-correlation with the rich photometric and spectroscopic redshift information available for foreground galaxies in the COSMOS field.

Prior to the CLAMATO survey, Lyα forest tomography was considered to only be feasible with future 30+m class telescopes. We have now, however, shown that the technique is in fact accessible to 8–10 m class telescopes, enabling the mapping of the $z \sim 2$–3 IGM absorption on comoving scales of ~ 2–3 h^{-1} Mpc. This demonstration is particularly exciting in the context of the various wide-field spectroscopic facilities on 8–10 m telescopes that are either being built, e.g., the Prime Focus Spectrograph (PFS) on the 8.2 m *Subaru* Telescope (Sugai et al. 2015), or in various stages of planning and discussion, e.g., the 11.25 m Maunakea Spectroscopic Explorer (MSE, McConnachie et al. 2016b). These facilities, which offer multiplex factors of several thousand over ~ 1deg^2 fields of view, should be able to carry out IGM tomography over much larger areas of tens or hundreds of square degrees, enabling new science cases at $z \sim 2$–3 with unprecedented statistical power.

Looking further into the 2020s, 30+m class facilities (Evans et al. 2012; Skidmore et al. 2015) would be required to push the spatial resolution of IGM tomography to comoving scales of 1 h^{-1} Mpc and below. As Lee et al. (2014a) calculated, not only do the densities of background sightlines need to increase, but the minimum pixel signal-to-noise also needs to be improved, as these scales are no longer in the shot-noise-dominated regime. The amount of photons that need to be collected in this regime increases exponentially as smaller mapping scales are desired, necessitating 30+m apertures.

Finally, the 2030s could see a dedicated "hyper-multiplexed" ($>10^4$ multiplex) wide-field spectroscopic facility such as the Billion Object Apparatus (BOA, Dodelson et al. 2016) on a 10m-class survey telescope. While BOA will not represent a large leap in collecting area compared to *Subaru*-PFS or MSE, its hyper-multiplexing will enable it to simultaneously carry out an all-sky galaxy redshift survey out to $z \sim 1.5$–2, and at the same time carry out an IGM tomography survey with similar parameters as CLAMATO, but over ~ 10000 deg^2. The goal of such a survey would be to map all cosmological linear modes out at $0 \lesssim z \lesssim 3$ in order to push cosmological parameter constraints beyond the LSST and DESI "Stage IV" limits.

CLAMATO, and its pioneering analyses, will be needed to pave the path for these ambitious projects of the future.

We thank Suk Sien Tie for pointing out some bugs in our initial data release. K.G.L. acknowledges support for this work by NASA through Hubble Fellowship grant HF2-51361 awarded by the Space Telescope Science Institute, which is operated by the Association of Universities for Research in Astronomy, Inc., for NASA, under contract NAS5-26555. We are also grateful to the entire COSMOS collaboration for their assistance and helpful discussions. The data presented herein were obtained at the W.M. Keck Observatory, which is operated as a scientific partnership among the California Institute of Technology, the University of California and the National Aeronautics and Space Administration (NASA). The Observatory was made possible by the generous financial support of the W.M. Keck Foundation. The authors also wish to recognize and acknowledge the very significant cultural role and reverence that the summit of Maunakea has always had within the indigenous Hawai'ian community. We are most fortunate to have the opportunity to conduct observations from this mountain.

Appendix A
Data Release

We have made the first data release of the Keck-CLAMATO data publicly available at doi:10.5281/zenodo.1292459. These include the reduced spectra, continuum-normalized Lyα forest pixels used as the input for the tomographic reconstruction, and the tomographic map of the $2.05 < z < 2.55$ IGM.

The 437 blue and 185 red reduced LRIS spectra are in FITS format, each with the following extensions:

1. HDU0: Object spectral flux density, in units of 10^{-17} ergs s^{-1} cm^{-2} Å^{-1}
2. HDU1: Noise standard deviation
3. HDU2 Pixel Wavelengths in angstroms

On the data webpage, we have provided an ASCII catalog that contains the information in Table 2, as well as the corresponding file names of the blue and red spectra for each object. We note that the spectrophotometry, especially in the red, might be unreliable.

We also provided a binary file with the intermediate product of 64,332 concatenated Lyα forest pixels (Equation (1)) at $2.05 < z_\alpha < 2.55$ from 240 background sources that satisfy our redshift and signal-to-noise criteria. This file includes the δ_f values and associated pixel noise, as a function of the $[x, y, z]$ positions relative to our tomographic map grid. The x and y coordinates correspond to transverse comoving distance along R.A. and decl., respectively, with the origins at $[\alpha_0, \delta_0] = [9^h59^m47\overset{s}{.}999, +02°9'0\overset{''}{.}00]$ (J2000) or $[\alpha_0, \delta_0] = [149\overset{°}{.}9500, 2\overset{°}{.}1500]$, while z corresponds to the line-of-sight comoving distance relative to the origin redshift of $z_\alpha = 2.05$. As described in Section 4, we adopt a fixed conversion between comoving distance and redshift, evaluated at our median map redshift of $\langle z \rangle = 2.30$. With our choice of cosmology, this yields $\chi = 3874.867\ h^{-1}$ Mpc and $d\chi/dz = 871.627\ h^{-1}$ Mpc. This intermediate binary file is the primary input used for the Wiener reconstruction algorithm to create the tomographic map.

The primary products are the binary files containing the IGM tomographic map, which spans comoving dimensions of $30\ h^{-1}$ Mpc $\times$ $24\ h^{-1}$ Mpc $\times$ $438\ h^{-1}$ Mpc in the $[x, y, z]$ dimensions, respectively, with binning in units of $0.5\ h^{-1}$ Mpc. The standard deviations ($\mathrm{Var}^{1/2}(\delta_F^{\mathrm{rec}})$) of the reconstruction (Equation (4)) are provided in a separate file with the same spatial binning and format. The conversion of the map coordinates back to R.A., decl. and redshift can be carried out with with the aforementioned χ and $d\chi/dz$ values. We provide both the direct tomographic reconstruction of the data, as well as a version that has been Gaussian-smoothed with a $\sigma = 2\ h^{-1}$ Mpc kernel; the latter is the version shown in the visualizations in Figures 10 and 11.

Appendix B
Three-dimensional Visualizations

We used the Blender software[33] to create a three-dimensional video of the tomographic maps presented in this paper. While it is not a commonly used tool for scientific visualization, Blender offers superior scene design and camera handling to most scientific visualization packages. Because our tomographic map consists only of scalar values, we can apply direct volume rendering such that each density value is mapped to a particular color and opacity value via a transfer function. To accomplish this, we make use of Blender's internal render engine where scalar values on a Cartesian grid can be represented as voxel data and the transfer function can be defined using a color ramp. The galaxies are represented by small spheres that all have the same size—in the future, we will aim to incorporate the morphologies and colors of the individual galaxies into the visualization. We have also created a 360-degree video that is compatible with the YouTube 360 Video API or planetarium projectors. As the internal render engine in Blender has no full-sky camera, we have to render six orthogonal camera images per frame for each camera position, with each camera's field of view set to 90deg × 90deg. All six images are then assembled into a so-called cube-map image that is subsequently mapped to a equirectangular projection as needed for 360deg videos by means of a small OpenGL program.

This video can viewed in the online version of Figure 10, while a spherically projected version has been uploaded to YouTube[34] that can be displayed with their 360 Video API, which allows the viewer to pan the viewing angle on most common web browsers by clicking and dragging with a mouse or trackpad. For users viewing the video with the Android or iOS YouTube smartphone application, this also exploits smartphone gyroscopes and accelerometers to offer a limited virtual-reality (VR) experience in conjunction with affordable stereoscopic headsets compatible with Google Cardboard. The viewer can turn his or her head to vary the camera viewpoint over the three rotational degrees of freedom (yaw, roll, and pitch) but not the three translational degrees.

Figure 11 shows another alternative method of viewing the 3D map: an interactive online X3D figure (Vogt et al. 2016), which allows readers of the online version to pan and zoom the map viewpoint within their web browser. The rendering capabilities of the X3D pathway are somewhat more limited than the Blender software used to create the video in that it cannot render a complicated transfer function of the map opacity, so we have only chosen to show two isodensity contours at $\delta_F^{\rm rec} = -0.08$ and $\delta_F^{\rm rec} = -0.18$, the former as a transparent blue layer and the latter as opaque, along with the positions of the coeval galaxies.

ORCID iDs

Khee-Gan Lee https://orcid.org/0000-0001-9299-5719
Alex Krolewski https://orcid.org/0000-0003-2183-7021
Martin White https://orcid.org/0000-0001-9912-5070
David Schlegel https://orcid.org/0000-0002-5042-5088
Peter E. Nugent https://orcid.org/0000-0002-3389-0586
Joseph F. Hennawi https://orcid.org/0000-0002-7054-4332
J. Xavier Prochaska https://orcid.org/0000-0002-7738-6875
Nao Suzuki https://orcid.org/0000-0001-7266-930X
Karl Glazebrook https://orcid.org/0000-0002-3254-9044
Jeyhan S. Kartaltepe https://orcid.org/0000-0001-9187-3605
Anton M. Koekemoer https://orcid.org/0000-0002-6610-2048
Christian Maier https://orcid.org/0000-0001-6405-2182
Themiya Nanayakkara https://orcid.org/0000-0003-2804-0648
D. B. Sanders https://orcid.org/0000-0002-1233-9998
Mara Salvato https://orcid.org/0000-0001-7116-9303
Kim-Vy H. Tran https://orcid.org/0000-0001-9208-2143

[33] https://www.blender.org/
[34] https://youtu.be/QGtXi7P4u4g

References

Bautista, J. E., Busca, N. G., Guy, J., et al. 2017, A&A, 603, A12
Berry, M., Gawiser, E., Guaita, L., et al. 2012, ApJ, 749, 4
Busca, N. G., Delubac, T., Rich, J., et al. 2013, A&A, 552, A96
Cai, Z., Fan, X., Bian, F., et al. 2017, ApJ, 839, 131
Cai, Z., Fan, X., Peirani, S., et al. 2016, ApJ, 833, 135
Capak, P., Aussel, H., Ajiki, M., et al. 2007, ApJS, 172, 99
Casey, C. M., Cooray, A., Capak, P., et al. 2015, ApJL, 808, L33
Caucci, S., Colombi, S., Pichon, C., et al. 2008, MNRAS, 386, 211
Chiang, Y.-K., Overzier, R. A., Gebhardt, K., et al. 2015, ApJ, 808, 37
Cisewski, J., Croft, R. A. C., Freeman, P. E., et al. 2014, MNRAS, 440, 2599
Croft, R. A. C., Romeo, A., & Metcalf, R. B. 2017, arXiv:1706.07870
Croft, R. A. C., Weinberg, D. H., Katz, N., & Hernquist, L. 1998, ApJ, 495, 44
Davidzon, I., Ilbert, O., Laigle, C., et al. 2017, arXiv:1701.02734
Dawson, K. S., Schlegel, D. J., Ahn, C. P., et al. 2013, AJ, 145, 10
Delubac, T., Bautista, J. E., Busca, N. G., et al. 2015, A&A, 574, A59
Diener, C., Lilly, S. J., Ledoux, C., et al. 2015, ApJ, 802, 31
Dodelson, S., Heitmann, K., Hirata, C., et al. 2016, arXiv:1604.07626
D'Odorico, V., Viel, M., Saitta, F., et al. 2006, MNRAS, 372, 1333
du Mas des Bourboux, H., Le Goff, J.-M., Blomqvist, M., et al. 2017, arXiv:1708.02225
Eisenstein, D. J., Weinberg, D. H., Agol, E., et al. 2011, AJ, 142, 72
Evans, C. J., Barbuy, B., Bonifacio, P., et al. 2012, Proc. SPIE, 8446
Faucher-Giguère, C., Prochaska, J. X., Lidz, A., Hernquist, L., & Zaldarriaga, M. 2008, ApJ, 681, 831
Font-Ribera, A., Arnau, E., Miralda-Escudé, J., et al. 2013, JCAP, 5, 18
Font-Ribera, A., McDonald, P., Mostek, N., et al. 2014, JCAP, 5, 23
Font-Ribera, A., Miralda-Escudé, J., Arnau, E., et al. 2012, JCAP, 11, 59
Hammer, F., Morris, S., Kaper, L., et al. 2016, Proc. SPIE, 9908, 990824
Ilbert, O., Capak, P., Salvato, M., et al. 2009, ApJ, 690, 1236
Jasche, J., Leclercq, F., & Wandelt, B. D. 2015, JCAP, 1, 036
Kirkby, D., Margala, D., Slosar, A., et al. 2013, JCAP, 3, 024
Koekemoer, A. M., Aussel, H., Calzetti, D., et al. 2007, ApJS, 172, 196
Kriek, M., Shapley, A. E., Reddy, N. A., et al. 2015, ApJS, 218, 15
Krolewski, A., Lee, K.-G., Lukić, Z., & White, M. 2017, ApJ, 837, 31
Krolewski, A., Lee, K.-G., White, M., et al. 2018, ApJ, 861, 60
Laigle, C., McCracken, H. J., Ilbert, O., et al. 2016, ApJS, 224, 24
Le Fèvre, O., Tasca, L. A. M., Cassata, P., et al. 2015, A&A, 576, A79
Lee, K.-G. 2018, kheegan/tomo_mapsn: IGM Tomography Analytic Forecasting Code, v1.0, Zenodo, doi:10.5281/zenodo.1293048
Lee, K.-G., Bailey, S., Bartsch, L. E., et al. 2013, AJ, 145, 69
Lee, K.-G., Hennawi, J. F., Stark, C., et al. 2014b, ApJL, 795, L12
Lee, K.-G., Hennawi, J. F., White, M., et al. 2016, ApJ, 817, 160
Lee, K.-G., Hennawi, J. F., White, M., Croft, R. A. C., & Ozbek, M. 2014a, ApJ, 788, 49
Lee, K.-G., Suzuki, N., & Spergel, D. N. 2012, AJ, 143, 51
Lee, K.-G., & White, M. 2016, ApJ, 831, 181
Lilly, S. J., Le Fèvre, O., Renzini, A., et al. 2007, ApJS, 172, 70
McConnachie, A., Babusiaux, C., Balogh, M., et al. 2016a, arXiv:1606.00043
McConnachie, A. W., Babusiaux, C., Balogh, M., et al. 2016b, arXiv:1606.00060
McDonald, P., Seljak, U., Burles, S., et al. 2006, ApJS, 163, 80
Metcalf, R. B., Croft, R. A. C., & Romeo, A. 2017, arXiv:1706.08939
Momcheva, I. G., Brammer, G. B., van Dokkum, P. G., et al. 2016, ApJS, 225, 27
Nanayakkara, T., Glazebrook, K., Kacprzak, G. G., et al. 2016, ApJ, 828, 21
Oke, J. B., Cohen, J. G., Carr, M., et al. 1995, PASP, 107, 375
Ozbek, M., Croft, R. A. C., & Khandai, N. 2016, MNRAS, 456, 3610

Palanque-Delabrouille, N., Magneville, C., Yèche, C., et al. 2013a, A&A, 551, A29
Palanque-Delabrouille, N., Yèche, C., Borde, A., et al. 2013b, A&A, 559, A85
Pâris, I., Petitjean, P., Rollinde, E., et al. 2011, A&A, 530, A50
Pichon, C., Vergely, J. L., Rollinde, E., Colombi, S., & Petitjean, P. 2001, MNRAS, 326, 597
Rakic, O., Schaye, J., Steidel, C. C., & Rudie, G. C. 2011, MNRAS, 414, 3265
Reddy, N. A., Steidel, C. C., Pettini, M., et al. 2008, ApJS, 175, 48
Rockosi, C., Stover, R., Kibrick, R., et al. 2010, Proc. SPIE, 7735, 77350R
Rollinde, E., Petitjean, P., Pichon, C., et al. 2003, MNRAS, 341, 1279
Schmittfull, M., & White, M. 2016, MNRAS, 463, 332
Scoville, N., Aussel, H., Brusa, M., et al. 2007, ApJS, 172, 1
Shapley, A. E., Steidel, C. C., Pettini, M., & Adelberger, K. L. 2003, ApJ, 588, 65
Skidmore, W. & TMT International Science Development Teams & Science Advisory Committee, T. 2015, RAA, 15, 1945
Slosar, A., Font-Ribera, A., Pieri, M. M., et al. 2011, JCAP, 9, 1
Slosar, A., Iršič, V., Kirkby, D., et al. 2013, JCAP, 4, 26
Sorini, D., Oñorbe, J., Hennawi, J. F., & Lukić, Z. 2017, arXiv:1709.03988
Spitler, L. R., Labbé, I., Glazebrook, K., et al. 2012, ApJL, 748, L21
Stark, C. W., Font-Ribera, A., White, M., & Lee, K.-G. 2015a, MNRAS, 453, 4311
Stark, C. W., White, M., Lee, K.-G., & Hennawi, J. F. 2015b, MNRAS, 453, 311
Steidel, C. C., Erb, D. K., Shapley, A. E., et al. 2010, ApJ, 717, 289
Steidel, C. C., Giavalisco, M., Pettini, M., Dickinson, M., & Adelberger, K. L. 1996, ApJL, 462, L17
Steidel, C. C., Shapley, A. E., Pettini, M., et al. 2004, ApJ, 604, 534
Straatman, C. M. S., Spitler, L. R., Quadri, R. F., et al. 2016, ApJ, 830, 51
Sugai, H., Tamura, N., Karoji, H., et al. 2015, JATIS, 1, 035001
Tytler, D., Kirkman, D., O'Meara, J. M., et al. 2004, ApJ, 617, 1
Vogt, F. P. A., Owen, C. I., Verdes-Montenegro, L., & Borthakur, S. 2016, ApJ, 818, 115
Wang, H., Mo, H. J., Yang, X., Jing, Y. P., & Lin, W. P. 2014, ApJ, 794, 94
Wang, T., Elbaz, D., Daddi, E., et al. 2016, ApJ, 828, 56